

Article

Skarn Formation and Zn–Cu Mineralization in the Dachang Sn Polymetallic Ore Field, Guangxi: Insights from Skarn Rock Assemblage and Geochemistry

Lei He ^{1,2,*}, Ting Liang ^{1,2,*}, Denghong Wang ^{3,*}, Jianxin Zhang ⁴ and Bosheng Liu ⁵¹ School of Earth Science and Resources, Chang'an University, Xi'an 710054, China; 2020027006@chd.edu.cn² Laboratory of Mineralization and Dynamics, Chang'an University, Xi'an 710054, China³ MNR Key Laboratory of Metallogeny and Mineral Assessment, Institute of Mineral Resources, Chinese Academy of Geological Sciences, Beijing 100037, China⁴ Northwest Bureau of China Metallurgical Geology Bureau, Xi'an 710119, China⁵ Guangxi 215 Geological Team Co., Ltd., Liuzhou 545002, China

* Correspondence: liangt@chd.edu.cn (T.L.); wangdenghong@vip.sina.com (D.W.)

Abstract: The Dachang is a world-class, super-giant Sn polymetallic ore field mainly composed of Zn–Cu ore bodies proximal to the granitic pluton and Sn polymetallic ore bodies distal to the granitic pluton. In this study, we used petrographic studies and major and trace element geochemistry with calc-silicates from the Zn–Cu ore bodies to constrain the physicochemical conditions of hydrothermal fluids during skarn rock formation and the evolution of ore-forming elements. Two skarn stages were identified based on petrographic observations: Prograde skarn rocks (Stage I), containing garnet, vesuvianite, pyroxene, wollastonite, and retrograde skarn rocks (Stage II), containing axinite, actinolite, epidote, and chlorite. The retrograde skarn rocks are closely associated with mineralization. The geochemical results show that the garnets in the Dachang ore field belong to the grossular–andradite solid solution, in which the early generation of garnet is mainly composed of grossular (average $\text{Gro}_{72}\text{And}_{25}$), while the later generation of garnet is mainly composed of andradite (average $\text{Gro}_{39}\text{And}_{59}$); the vesuvianites are Al-rich vesuvianites; the pyroxenes form a diopside–hedenbergite solid solution with a composition of $\text{Di}_{3-86}\text{Hd}_{14-96}$; the axinites are mainly composed of ferroaxinite; and the actinolites are Fe-actinolite. The mineral assemblage of the skarn rocks indicates that the ore-forming fluid was in a relatively reduced state in the early prograde skarn stage. As the ore-forming fluid evolved, the oxygen fugacity of the ore-forming fluid increased. During the final skarn stage, the ore-forming fluid changed from a relatively oxidized state to a reduced state. The skarn rocks have evolved from early Al-rich to late Fe-rich characteristics, indicating that the early ore-forming fluid was mainly magmatic exsolution fluid, which may mainly reflect the characteristics of magmatic fluids, and the late Fe-rich characteristics of the skarn rocks may indicate that the late hydrothermal fluid was strongly influenced by country rocks. Trace element analyses showed that the Sn content decreased from the prograde skarn stage to the retrograde skarn stage, indicating that Sn mineralization was not achieved by activating and extracting Sn from prograde skarn rocks by hydrothermal fluids. The significant enrichment of Sn in the magmatic hydrothermal fluid is a necessary condition for Sn mineralization. There are various volatile-rich minerals such as axinite, vesuvianite, fluorite, and tourmaline in the Dachang ore field, indicating that the ore-forming fluid contained extensive volatiles B and F, which may be the fundamental reason for the large-scale mineralization of the Dachang ore field.



Citation: He, L.; Liang, T.; Wang, D.; Zhang, J.; Liu, B. Skarn Formation and Zn–Cu Mineralization in the Dachang Sn Polymetallic Ore Field, Guangxi: Insights from Skarn Rock Assemblage and Geochemistry. *Minerals* **2024**, *14*, 193. <https://doi.org/10.3390/min14020193>

Academic Editor: Panagiotis Voudouris

Received: 11 January 2024

Revised: 8 February 2024

Accepted: 10 February 2024

Published: 12 February 2024



Copyright: © 2024 by the authors. Licensee MDPI, Basel, Switzerland. This article is an open access article distributed under the terms and conditions of the Creative Commons Attribution (CC BY) license (<https://creativecommons.org/licenses/by/4.0/>).

Keywords: skarn rock; Dachang; ore-forming fluid evolution

1. Introduction

Skarn deposits are one of the most important ore types in the Earth's crust and have been mined for a variety of metals, such as Cu, Fe, Mo, Zn, W, Sn, and Au, and mainly

occur at the contact zone between intermediate–acidic intrusions and carbonate rocks. The interactions between the hydrothermal fluids and the country rocks have produced a sequence of skarn rocks that record the migration directions of the hydrothermal fluids and the evolution of mineralization during the formation of the skarn deposits. They are an ideal model for studying element migration in hydrothermal fluids [1–5].

The Dachang in Guangxi is a world-class, super-giant Sn polymetallic ore field, mainly composed of Zn–Cu ore bodies proximal to the granitic pluton and Sn polymetallic ore bodies distal to the granitic pluton, with Sn reserves of over 1 million tons (average grade 1%) and Zn reserves of 4.5 million tons (average grade 4%), accompanied by Cu, Pb, Sb, As, In, and Ge [6]. The Zn–Cu ore bodies mainly occur in the central part of the ore field and the deep part of Changpo–Tongkeng adjacent to the granitic pluton. The Sn polymetallic ore bodies mainly occur in the western and eastern parts of the ore field distal to the granitic pluton. Numerous isotopic geochronology studies have shown that the mineralization ages of the Sn polymetallic and Zn–Cu ore bodies were consistent with the emplacement age of the Longxianggai granitic pluton [7–14]. Previous researchers have carried out extensive studies here, but the focus of previous work has mainly been on the genesis of deposits, emplacement ages of granitic pluton, metallogenic age and isotopic studies, etc. [7–24]. However, mineralogical research, especially systematic studies of skarn rock petrography and geochemistry, is still relatively weak, which restricts the improvement of deposit models and in-depth understanding of skarn mineralization.

Based on previous studies, detailed petrographic observations and major element analyses were carried out on prograde skarn rocks (garnet, wollastonite, vesuvianite, pyroxene) and retrograde skarn rocks (axinite, actinolite, epidote), and representative skarn minerals (garnet, axinite) from different stages were selected for trace element analyses to constrain the physicochemical conditions of the hydrothermal fluids during skarn rock formation and the evolution of ore-forming elements.

2. Geological Setting

The Dachang ore field is located in the central part of the important non-ferrous metal mineralization belt in China, the Danchi metallogenic belt, at the junction of the Paleotethys tectonic domain and the Pacific tectonic domain (Figure 1). The outcropping strata in the study area are mainly composed of Devonian mudstone, marl, and siliceous rocks, with a small amount of Carboniferous limestone. Among them, the Devonian strata are the main host rocks of the deposit [15,22]. The lithology, from bottom to top, is as follows: Black mudstone, shale and reef limestone in the lower part of the middle Devonian Nabiao Formation (D_2^{nb}); thick stratiform limestone, black mudstone and shale of the Luofu Formation (D_2^l) in the upper part of the middle Devonian, with locally lenticular carbonaceous pitch; banded siliceous rocks with calcareous nodules of the Liujiang Formation (D_3^l) in the lower part of the upper Devonian; limestone of the Wuzhishan Formation (D_3^w) in the middle part of the upper Devonian, which can be further divided into four sublayers from bottom to top: thick-striped limestone ($D_3^w^a$), thin-striped limestone ($D_3^w^b$), small lenticular limestone ($D_3^w^c$) and large lenticular limestone ($D_3^w^d$); carbonate rocks and shale of the Tongchejiang Formation (D_3^t) in the upper part of the upper Devonian; and quartz sandstone, mudstone and carbonaceous shale of the Simen Formation (C_1s) in the lower Carboniferous (Figure 2).

The structures in the ore field are mainly composed of the NW-trending Danchi and Dachang faults and anticlines, overlain by the later NE- and SN-trending folds, faults, and fractures [6].

Magmatic activity in the Dachang ore field is relatively active, and granitic plutons are less exposed on the surface and mainly occur as concealed plutons. The Longxianggai granitic pluton is the main magmatic intrusion in the study area, which crops out in the central part of the Dachang ore field, and it extends westward to the Changpo–Tongkeng deposit in the deep part [7]. The granitic pluton is mainly composed of medium- to coarse-grained biotite granite, fine-grained granite, and porphyritic biotite granite, with a gradual

spatial transition relationship. The zircon U–Pb isotopic chronology of the Longxianggai granitic pluton ranges from 96.6 to 88.8 Ma [7,10,14,18]. In the eastern and western parts of the Changpo–Tongkeng, SN-trending granite porphyry and diorite porphyrite dikes intruded between 91.0 and 85.8 Ma [14,18].

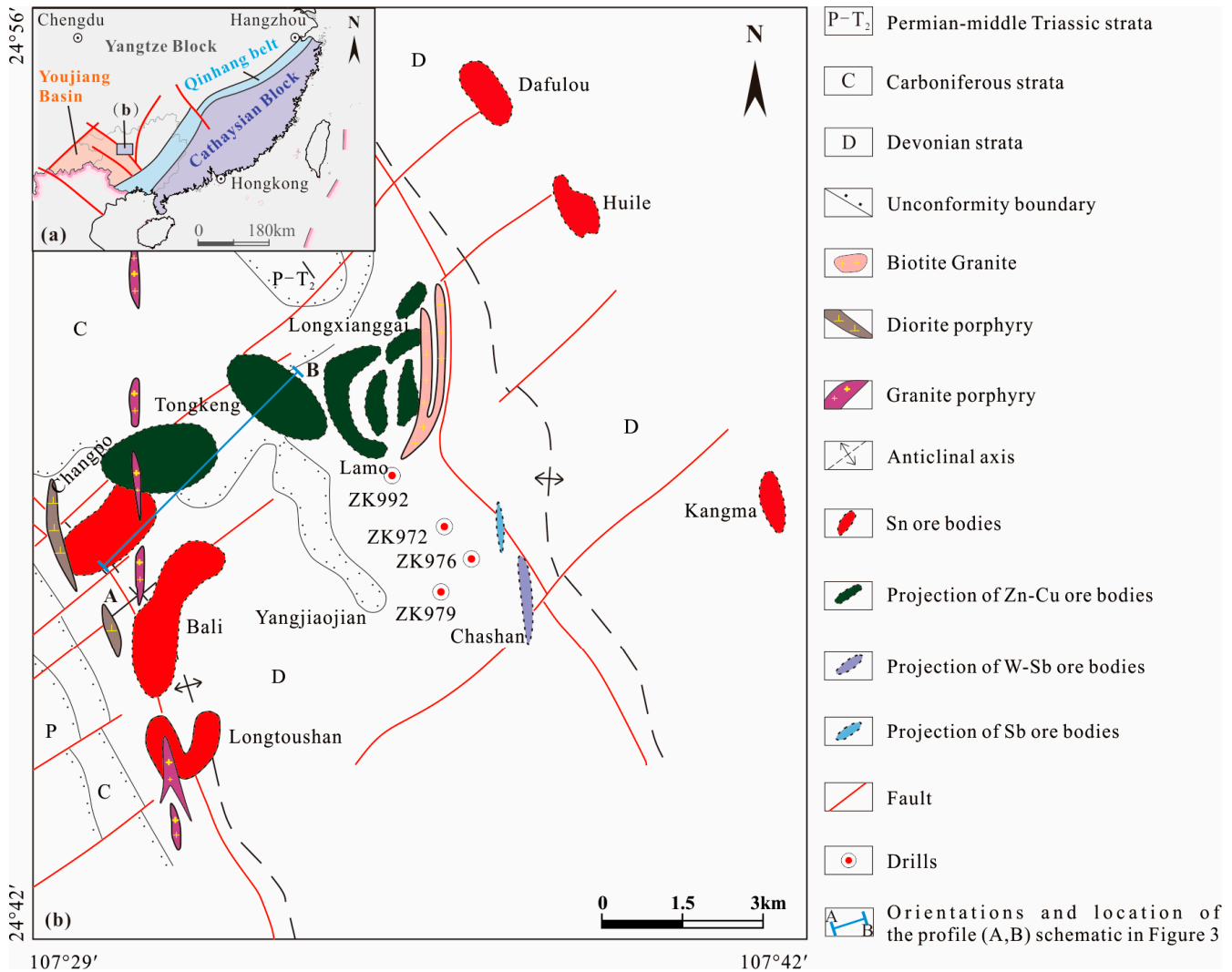


Figure 1. Location diagram of Dachang ore field (a) and distribution of deposits in Dachang ore field (b) (modified after [15]).

The Dachang ore field is divided into three zones surrounding the Longxianggai granite. The western zone is represented by the Changpo–Tongkeng and Bali–Longtoushan Sn polymetallic deposits, while the central zone mainly includes the Lamo Zn–Cu and Chashan W–Sb deposits. There are some small- and medium-sized Sn polymetallic deposits in the eastern zone (such as Dafulou, Huile, and Kangma).

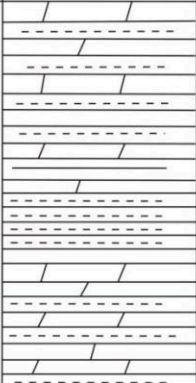
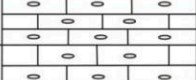
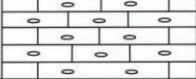
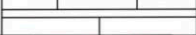
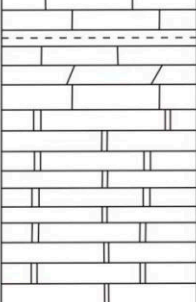
	Formation	Stratigraphy	Lithology	Orebody	
Upper Devonian	Tongchejiang Formation		Carbonaceous shale, mudstone		
			Carbonaceous mudstone, shale and interbedded silty mudstone		
	Wuzhishan Formation	$D_3^d W$		Limestone with big lenticular	Changpo-Tongkeng Sn polymetallic ore bodies Lamo Zn-Cu deposit
		$D_3^c W$		Limestone with small lenticular	
		$D_3^b W$		Thin-striped siliceous limestone	
$D_3^a W$			Thick-striped siliceous limestone		
	Liujiang Formation D_3^l		Black siliceous shale, siliceous rock		
Lower Devonian	Luofu Formation		Thick layered limestone interbedded with mudstone and shale, with locally containing carbonaceous pitch Clastic rock, carbonaceous shale, mudstone, with a bottom of siltstone or sandstone	Changpo-Tongkeng Zn-Cu ore bodies	

Figure 2. Stratigraphic column of the Dachang ore field (modified after [8]).

3. Geology of the Deposit

The Sn polymetallic deposit is the largest and most representative deposit in the Dachang ore field, mainly consisting of stratiform and vein-shaped ore bodies. The ore minerals are mainly composed of cassiterite, pyrite, sphalerite, pyrrotite, arsenopyrite, and jamesonite, with complex mineral assemblages. The gangue minerals are quartz, calcite, and tourmaline.

The size of the W-Sb deposit is smaller than that of the Zn–Cu and Sn polymetallic deposits, which mainly consist of vein-shaped ore bodies. The mineral assemblages are simple and consist mainly of stibnite, wolframite, and scheelite. The gangue minerals are calcite, fluorite, and quartz.

The skarn Zn–Cu deposit mainly consists of the Lamo Zn–Cu deposit in the central part of the Dachang ore field and the lower part of the Changpo–Tongkeng deposit in the western part adjacent to the granitic pluton (Figure 3).

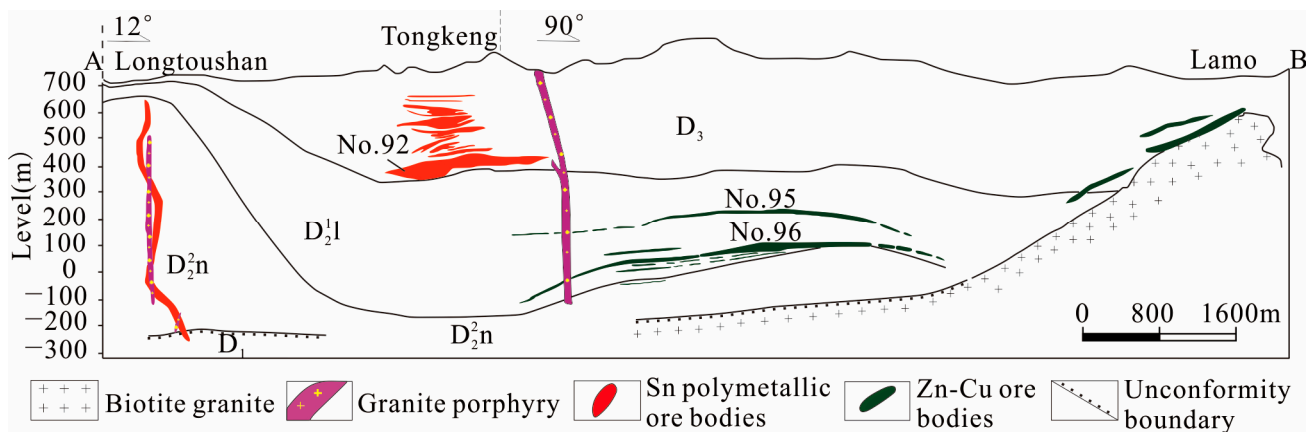


Figure 3. Profile of the Sn polymetallic ore bodies and Zn–Cu ore bodies distribution in the Dachang ore field (modified after [20]).

3.1. Lamo Zn–Cu Deposit

The Lamo Zn–Cu deposit is located at the contact zone between the outcrop of the Longxianggai granite and the upper Devonian striped limestone and small lenticular limestone in the central part of the Dachang ore field. It consists of gently dipping stratiform-like ore bodies and steeply dipping vein-shaped ore bodies. Among them, the gently dipping stratiform-like ore bodies are the main industrial ore bodies. The stratiform-like ore bodies are conformable with the host rock, with a strike of NNW, dipping NE, and the dip angle is relatively gentle, which mainly includes the No. 0, No. 1, and No. 3 ore bodies. The No. 0 ore body is the largest, with a strike length of 1365 m and an average thickness of 3.81 m. The No. 1 ore body extends for 130 m along strike and 4.32 m in depth. The No. 3 ore body extends for 80 to 160 m along strike, with an average thickness of 10.33 m. The vein-shaped ore bodies crop out in the cutting layer, with a strike of 15° to 25° and a dip of 285° to 295° . The dip angle is relatively steep, and mineralization is mainly characterized by filling and metasomatism along fractures, mainly including the No. 11, No. 12, No. 13, and No. 14 ore bodies. The ore bodies are large in size and stable in extension [25].

3.2. Lower Part of the Changpo–Tongkeng Deposit

The Zn–Cu ore bodies crop in the contact zone between the concealed Longxianggai granitic pluton and the calcareous mudstone and marl of the middle Devonian Luofu Formation (D_2^l). There are three roughly parallel stratiform ore bodies, No. 94, No. 95, and No. 96 (Figure 4), with ore bodies striking 58° to 65° and dipping 328° to 335° [16]. The No. 94 ore body extends for 140 to 400 m along strike and 0.52 to 20 m in depth. The No. 95 ore body extends for 1500 m along strike and 0.66 to 31.76 m in depth. The No. 96 ore body has a strike length of 2235 m and an average thickness of 8.74 m.



Figure 4. Characteristics of mineral assemblages in Zn–Cu ore bodies. (a) Zn–Cu ore bodies and garnet bands along layers, (b) contact relationship between skarn rocks and granitic pluton, (c) the retrograde skarn stage is intimately related to mineralization.

The mineral assemblage of the Zn–Cu ore bodies includes sphalerite, chalcopyrite, arsenopyrite, pyrrhotite, and pyrite, while the gangue minerals are mainly calc-silicates, fluorite, calcite, quartz, and tourmaline. Massive and disseminated structures predominate, forming zoning, subhedral–anhedral and exsolution textures.

The host rock proximal to the granitic pluton has undergone thermal metamorphism to form marble and hornfels and metasomatism to form skarns. Skarnization is closely related to mineralization and is a prospecting indicator. Based on mineralogical characteristics and mineral assemblages, the skarn can be divided into two stages. The prograde skarn stage (stage I) is dominated by garnet, vesuvianite, pyroxene, and wollastonite, while the retrograde skarn stage (stage II) is dominated by axinite, actinolite, epidote, chlorite, and other hydrated silicate minerals. The retrograde skarn stage is intimately related to mineralization.

Based on the spatial distribution, occurrence characteristics, and mineral assemblages, the skarn Zn–Cu mineralization can be divided into two stages and four sub-stages (Figure 5). These stages include the skarn stage and the sulfide stage.

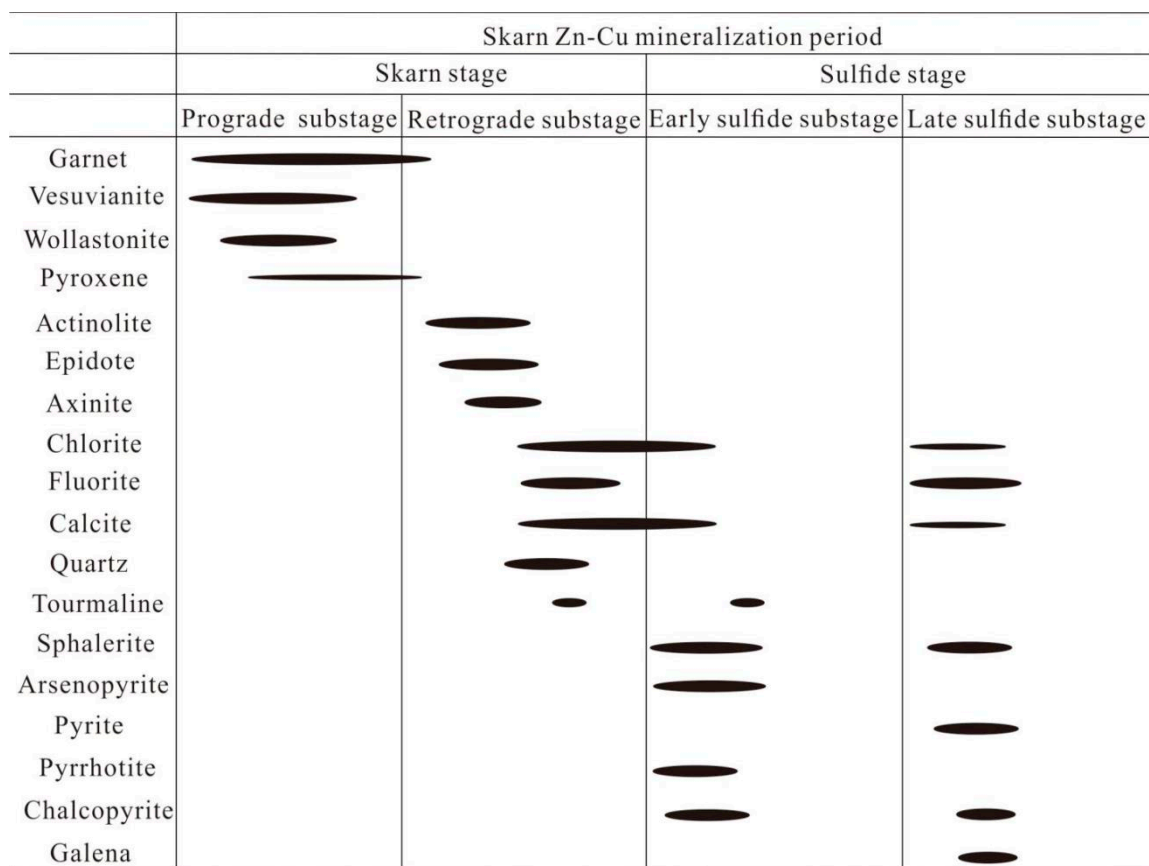


Figure 5. Paragenesis of the mineral assemblages showing the mineralized sequence of Zn–Cu ore bodies.

4. Sampling and Analytical Methods

The samples used for analysis were collected from the host rocks of the Zn–Cu ore bodies. Based on field geological surveys and microscopic observations, typical skarn rocks (garnet, vesuvianite, wollastonite, pyroxene, actinolite, axinite, and epidote) were selected for electron probe microanalysis (EPMA). The prograde skarn rock garnet and the retrograde skarn rock axinite were selected for laser ablation inductively coupled plasma mass spectrometry (LA-ICP–MS) trace element analysis. All sample analyses were completed at the Laboratory of Mineralization and Dynamics, Chang’an University.

Major element analyses were carried out on an EPMA (JXA-iHP200F) with an acceleration voltage of 15 kV, a beam current of 10 nA, and a beam spot diameter of 1 μm . In this work, the natural minerals albite, forsterite, corundum, K-feldspar, apatite, chromite, fayalite, and cassiterite were used as standards for Na, Mg, Al, K, P, Cr, Fe, and Sn, respectively. The natural mineral wollastonite was used as a standard for Si and Ca, and pyrophanite was used for Mn and Ti. Nickel oxide was used as the standard for Ni. Here, the element concentrations were calculated using the CitZAF interelement correction model [26].

Trace element quantification was performed by an Agilent 7900 quadrupole ICP-MS coupled with an ESL 193HE excimer laser ablation system. He (flow rate 0.5 L/min) was used as the carrier gas, and Ar (flow rate 0.8 L/min) as the make-up gas, with a beam diameter of 35 μm , a laser repetition rate of 11 HZ, and an energy fluence of 6.4 J/cm². Each analysis included a background measurement for 25 s, followed by 40 s of data acquisition. The NIST SRM 610 silicate glass standard was used for external calibration. Here, one complete assay cycle contained a sequence of 2 spot analyses of NIST SRM 610, 6 to 10 spot analyses of unknown samples, and 2 spot analyses of NIST SRM 610. All data were collected in time-resolved analysis (TRA) mode, and data reduction was performed using “Stalquant”, an in-house data reduction software developed by the Günther group at ETH [27]. Quantification was performed using Si as the internal standard element or via matrix normalization (100 wt% oxides) [28].

5. Results

5.1. Petrographic Characteristics and EPMA Analysis Results

5.1.1. Garnet

Garnet coexists with vesuvianite and metasomatized the muddy-rich zone in the original rock. It is the earliest-formed and dominant skarn mineral, cut by vesuvianite-calcite veins and pyroxene-calcite veins, and replaced by later-formed pyroxene, epidote, and calcite. The garnet in the hand specimen shows a light brownish-red color (Figure 6a–c), with an euhedral–subhedral texture and grain sizes ranging from 0.6 to 5 mm. Under plane-polarized light, the garnet is colorless to light brown. Based on hand specimens and microscopic observations, the garnet can be divided into two generations: An early generation (Grt I) and a late generation (Grt II). Grt I displays a euhedral–subhedral dodecahedral texture, homogeneous or local abnormal extinction, and a lack of well-developed zoning. It is often intergrown with wollastonite, vesuvianite and pyroxene (Figure 6e,j,k). The surface of Grt I is relatively rough and has a dissolution texture; some surfaces can be seen to have been replaced by calcite and epidote, which may be a superposition of later hydrothermal alteration. Grt II is associated with sulfides or cuts through Grt I in a vein-like pattern (Figure 6f,g) with a euhedral–subhedral texture and obvious heterogeneity. Grt II showed well-developed zoning. Part of Grt II contains fine-grained pyroxene.

The EPMA results for two generations of garnets were published by He et al. [24]. The SiO₂ and CaO contents in the garnets show limited variation, ranging from 36.04 to 39.31 wt% and 33.62 to 35.84 wt%, respectively. Compared to Grt II, Grt I is rich in Al₂O₃ (10.47 to 19.08 wt%) and deplete in FeO (4.97 to 15.54 wt%). Grt II is relatively rich in FeO (14.10 to 18.67 wt%) and deplete in Al₂O₃ (7.91 to 11.53 wt%), with low content of TiO₂ and MnO. The data (based on 12 oxygen atoms) show that the garnet from the Dachang ore field belongs to the grossular–andradite solid solution series (Gro_{29–82}And_{12–69}); Grt I is Al-rich and dominated by grossular, while Grt II is Fe-rich and dominated by andradite (Figure 7a).

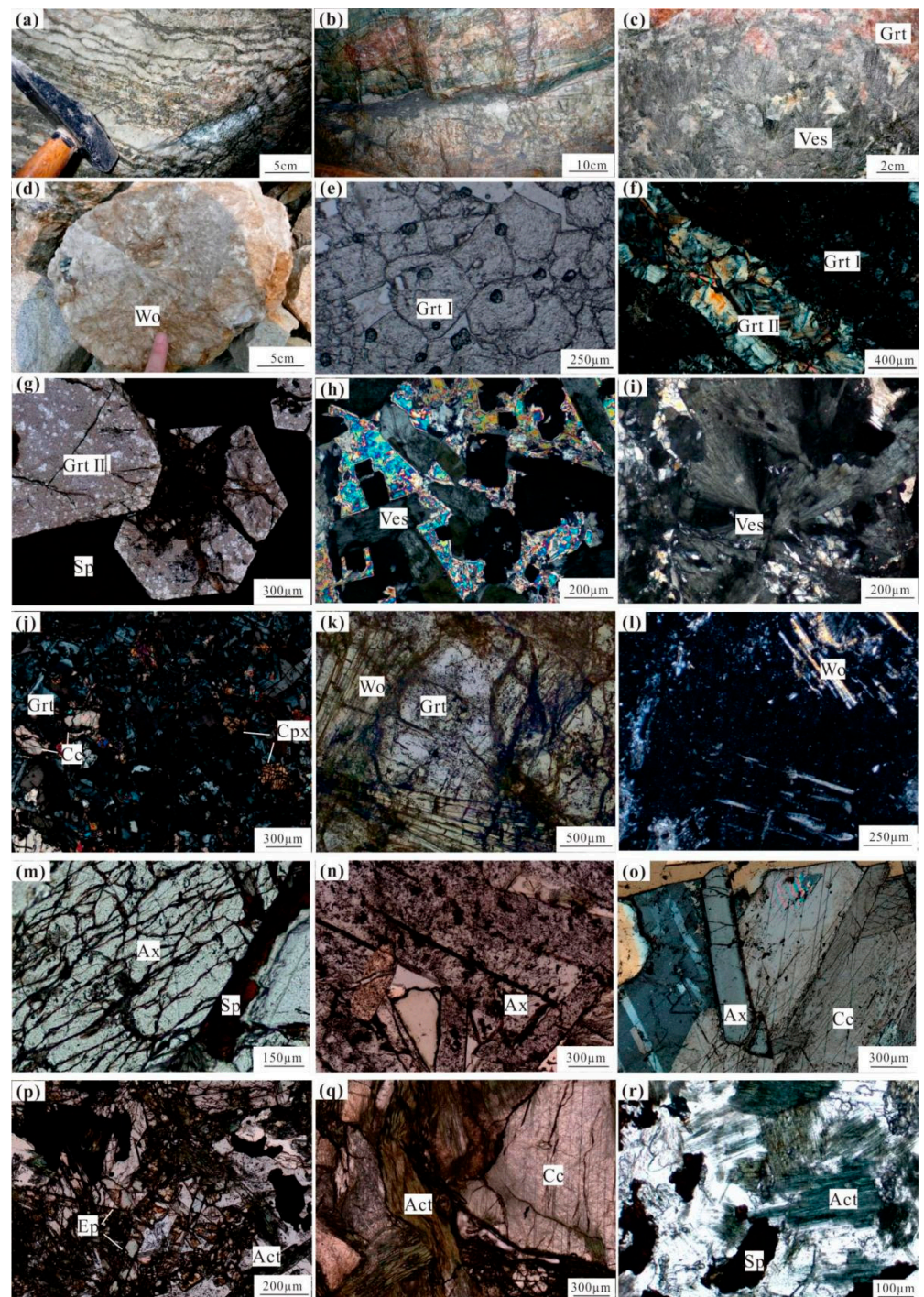


Figure 6. Skarn mineral characteristics of Dachang ore field. (a) Sphalerite and garnet formed along strata, (b) skarn formation along strata, (c) vesuvianite intergrown with garnet, (d) wollastonite with radiated aggregate, (e) Grt I presents euhedral–subhedral grains with a rough surface, (f) Grt I cut by vein Grt II, (g) Grt II surrounded by sphalerite, (h) the interference color of vesuvianite is grayish-white, (i) vesuvianite with a radiated aggregate, (j) pyroxene included in garnet in an irregular granular form, (k) wollastonite intergrown with garnet, (l) long-prismatic wollastonite in carbonaceous siliceous rocks, (m) axinite surrounded by sphalerite, (n) plate-prismatic axinite, (o) axinite surrounded by calcite, (p) green granular epidote surrounded by actinolite, (q) actinolite with fibrous associated with calcite, and (r) actinolite coexisting with sphalerite. Mineral abbreviations: Grt—garnet, Ves—vesuvianite, Wo—wollastonite, Sp—sphalerite, Ep—epidote, Cpx—clinopyroxene, Ax—axinite, Cc—calcite, Act—actinolite.

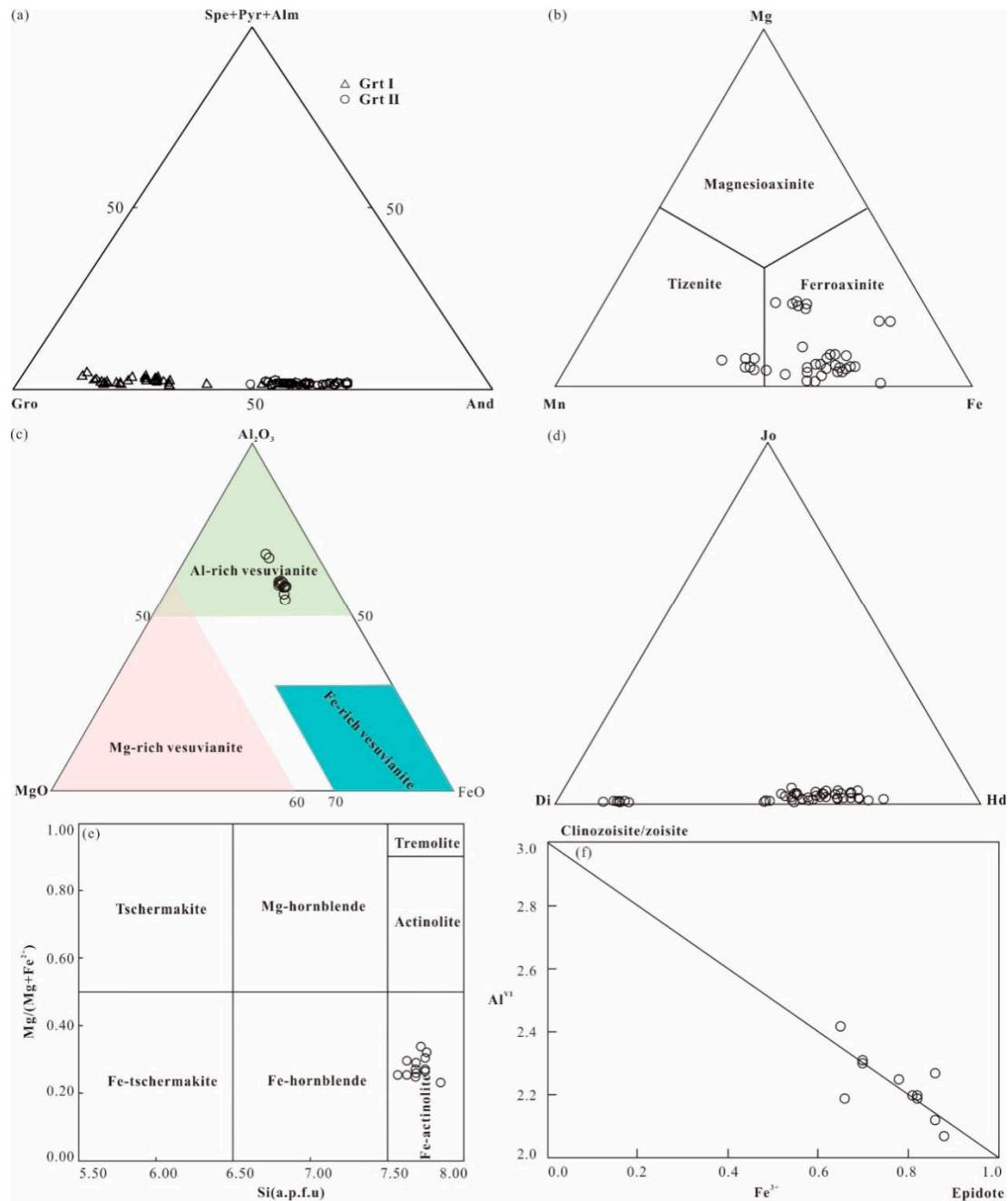


Figure 7. (a) Diagram of end members of garnet (after [29]), (b) diagram for classification of axinite (after [30]), (c) diagram for classification of vesuvianite (after [31,32]), (d) diagram of end members of clinopyroxene (after [5]), (e) diagram for classification of amphibole (after [33]), and (f) distribution of octahedral Al and Fe for epidotes (after [34]) from Dachang ore field. Mineral abbreviations: And— andradite, Gro—grossular, Spe—spessartine, Pyr—pyrope, Alm—almandine, Jo—johannsonite, Di—diopside, Hd—hedenbergite.

5.1.2. Vesuvianite

The vesuvianite content of the skarn rocks is relatively high and is seen in the field as a gray-green radiated aggregate coexisting with garnet (Figure 6c), formed in the prograde skarn stage. Under plane-polarized light, the vesuvianite is colorless with granular, columnar, and radial particles (Figure 6h,i) and considerable variation in particle size. The cross-section of the vesuvianite is square, and discontinuous stripes and bands are seen in the vertical section. The interference color is grayish-white, with an abnormal

interference color of grayish-yellow. Vesuvianite coexists with garnet in euhedral granules, while epidote in irregularly granular filled between garnet and vesuvianite.

The EPMA analysis results for the vesuvianite are shown in Table 1, and the SiO₂ content ranges from 35.23 to 36.76 wt% (avg. 36.06 wt%); CaO ranges from 34.88 to 37.12 wt% (avg. 35.94 wt%); Al₂O₃ ranges from 11.90 to 15.28 wt% (avg. 13.24 wt%); TFeO ranges from 4.11 to 6.72 wt% (avg. 5.77 wt%); MgO ranges from 2.65 to 3.12 wt% (avg. 2.84 wt%); TiO₂ ranges from 0.14 to 0.23 wt% (avg. 0.18 wt%); and Cr₂O₃ ranges from 0.04 to 1.48 wt% (avg. 0.29 wt%). The contents of MnO, Na₂O, K₂O, NiO, and P₂O₅ are relatively low. A small amount of SnO₂ (0 to 0.02 wt%) is also detected in the vesuvianite. The vesuvianite classification diagram shows that the vesuvianite in the Dachang ore field is an Al-rich vesuvianite (Figure 7c).

5.1.3. Pyroxene

Pyroxene, which is a green irregular granule in the outcrop, is of low abundance compared with garnet and vesuvianite. Under plane-polarized light, it is colorless to green, while under cross-polarized light, the interference color is relatively high, reaching blue-green to orange-yellow, with developed cleavage (Figure 6j). Under the microscope, pyroxene is seen to occur as irregular grains filling interstices between vesuvianite and garnet, accompanied by wollastonite. It can also be seen that the pyroxene replaced garnet, which indicated that it formed slightly after the garnet and vesuvianite.

The EPMA results (Table 2) show that the pyroxene in the Dachang ore field belongs to the diopside–hedenbergite solid solution (Figure 7d). The SiO₂ content in the diopside is 52.00 to 55.03 wt%, CaO is 24.81 to 26.48 wt%, TFeO is 4.37 to 6.73 wt%, and MgO is 13.58 to 15.27 wt%; the contents of SiO₂ in the hedenbergite are 47.28 to 50.87 wt%, CaO are 22.65 to 24.60 wt%, TFeO are 17.98 to 28.16 wt%, and MgO are 0.44 to 6.54 wt%. The contents of MnO, Cr₂O₃, Na₂O, Al₂O₃, TiO₂, K₂O, NiO, and P₂O₅ in the pyroxene are relatively low. A small amount of SnO₂ (0 to 0.27 wt%) is also detected in the pyroxene.

The data (based on 6 oxygen atoms) show that the main end member of the pyroxene is hedenbergite (Hd), with a variation range of 13.82 to 95.54% (avg. 66.86%); the second end member is diopside (Di), with a variation range of 2.69 to 85.67% (avg. 30.85%); it also contains a small amount of johannsenite (Jo) with a content of <6%, belonging to the diopside–hedenbergite solid solution (Di_{3–86}Hd_{14–96}Jo_{0.5–6}).

5.1.4. Wollastonite

Wollastonite is one of the important minerals in the prograde skarn stage, and hand specimens are gray-white to pale red, long-prismatic, and radiated (Figure 6d), with a glassy luster. Under plane-polarized light, it is colorless, the interference color is gray to orange under cross-polarized light, and it coexists with pyroxene, garnet, and vesuvianite (Figure 6k). In some calcareous siliceous rocks, limestones, and marlstones, wollastonite is scattered in long-prismatic, radiated, and agglomerate.

The chemical composition of wollastonite is relatively simple, mainly consisting of SiO₂ and CaO. The EPMA results are shown in Table 3, with SiO₂ contents ranging from 49.71 to 51.92 wt% (avg. 50.81 wt%), CaO contents ranging from 46.32 to 49.98 wt% (avg. 48.42 wt%), and small amounts of NiO, TFeO, and Na₂O. The calculation shows that the end member component of the wollastonite is mainly wollastonite (Wo), with a range of 99.07 to 99.84% (avg. 99.52%), while the contents of enstatite (En), ferrosilite (Fs), and aegirine (Ac) are less than 1%. A small amount of SnO₂ (0 to 0.06 wt%) is also detected in wollastonite.

Table 1. Major element compositions (wt%) of the vesuviante.

Sample		Na ₂ O	K ₂ O	FeO	MgO	P ₂ O ₅	MnO	Al ₂ O ₃	CaO	NiO	SiO ₂	TiO ₂	Cr ₂ O ₃	SnO ₂	Total	Na	Fe	Mg	Mn	Al	Ca	Si	Ti	Cr
LM-21X (N = 5)	MAX	0.06	0.01	6.11	3.01	0.03	0.14	13.24	36.31	0.03	36.22	0.23	0.24	0.01	94.32	0.03	1.38	1.19	0.03	4.15	10.32	9.73	0.05	0.05
	MIN	0.01	0.00	5.69	2.65	0.00	0.04	11.90	35.40	0.00	35.23	0.14	0.04	0.00	92.78	0.01	1.27	1.07	0.01	3.77	10.11	9.43	0.03	0.01
	AVG	0.03	0.01	5.96	2.85	0.01	0.08	12.79	35.73	0.01	35.65	0.17	0.11	0.01	93.41	0.02	1.34	1.14	0.02	4.03	10.25	9.54	0.04	0.02
LM-15X (N = 4)	MAX	0.06	0.02	6.72	3.12	0.08	0.21	15.28	37.12	0.01	36.76	0.21	1.48	0.02	97.11	0.03	1.47	1.22	0.05	4.60	10.16	9.62	0.04	0.31
	MIN	0.02	0.00	4.11	2.70	0.01	0.10	12.31	34.88	0.00	35.97	0.16	0.09	0.00	94.27	0.01	0.90	1.05	0.02	3.80	9.80	9.37	0.03	0.02
	AVG	0.04	0.01	5.29	2.82	0.05	0.16	13.94	35.91	0.00	36.37	0.18	0.66	0.01	95.44	0.02	1.15	1.10	0.04	4.28	10.02	9.48	0.04	0.14
590-1X (N = 4)	MAX	0.04	0.01	6.11	2.88	0.02	0.10	13.36	36.47	0.01	36.64	0.19	0.26	0.01	95.48	0.02	1.34	1.12	0.02	4.12	10.25	9.60	0.04	0.06
	MIN	0.03	0.00	5.95	2.80	0.01	0.07	12.92	36.08	0.00	35.84	0.16	0.06	0.00	94.22	0.02	1.31	1.11	0.02	3.99	10.20	9.51	0.03	0.01
	AVG	0.04	0.00	6.01	2.85	0.02	0.09	13.12	36.25	0.01	36.25	0.18	0.15	0.01	94.96	0.02	1.32	1.12	0.02	4.07	10.22	9.54	0.04	0.03

Number of ions based on 38 oxygen atoms.

Table 2. Major element compositions (wt%) of the pyroxene.

Sample		SiO ₂	TiO ₂	Al ₂ O ₃	Cr ₂ O ₃	FeO	MnO	MgO	CaO	Na ₂ O	K ₂ O	NiO	SnO ₂	P ₂ O ₅	Total	Si	Fe ³⁺	Fe ²⁺	Mn	Mg	Ca	Jo	Di	Hd
976-500.53 (N = 3)	MAX	55.03	0.06	0.39	0.11	5.84	0.28	15.27	25.74	0.17	0.03	0.03	0.02	0.02	100.36	2.01	0.04	0.15	0.01	0.83	1.03	0.90	85.67	18.64
	MIN	52.96	0.01	0.16	0.05	4.37	0.15	14.17	24.81	0.05	0.01	0.01	0.02	0.02	99.13	1.98	0.00	0.13	0.00	0.79	0.97	0.50	80.86	13.82
	AVG	53.81	0.04	0.26	0.07	5.27	0.20	14.60	25.39	0.10	0.02	0.02	0.02	0.02	99.78	1.99	0.03	0.14	0.00	0.81	1.01	0.63	82.62	16.74
LM-4X (N = 4)	MAX	53.53	0.03	0.22	0.05	6.73	0.34	14.82	26.48	0.09	0.02	0.03	0.00	0.04	100.50	2.00	0.16	0.21	0.01	0.83	1.06	1.03	82.31	21.35
	MIN	52.00	0.01	0.09	0.02	5.11	0.17	13.58	25.07	0.02	0.02	0.01	0.00	0.03	98.44	1.94	0.00	0.04	0.01	0.77	1.02	0.55	78.10	16.76
	AVG	52.93	0.02	0.14	0.04	6.03	0.27	14.07	25.79	0.05	0.02	0.02	0.00	0.04	99.37	1.99	0.04	0.15	0.01	0.79	1.04	0.87	80.00	19.13
590-7 (N = 4)	MAX	50.35	0.01	0.27	0.07	23.51	0.85	4.94	24.04	0.14	0.01	0.04	0.00	0.01	100.83	2.00	0.10	0.79	0.03	0.29	1.02	2.81	29.42	81.72
	MIN	47.99	0.01	0.13	0.05	20.49	0.57	2.63	22.65	0.07	0.01	0.03	0.00	0.01	98.86	1.96	0.00	0.63	0.02	0.16	0.99	2.01	16.28	68.21
	AVG	49.18	0.01	0.20	0.06	22.34	0.72	3.69	23.37	0.10	0.01	0.04	0.00	0.01	99.68	1.99	0.04	0.71	0.03	0.22	1.01	2.46	22.17	75.38
590-21 (N = 4)	MAX	50.79	0.03	0.05	0.05	23.15	1.33	4.46	24.60	0.09	0.02	0.03	0.04	0.02	100.91	2.01	0.01	0.78	0.05	0.26	1.04	4.68	27.65	80.76
	MIN	49.29	0.01	0.04	0.04	19.76	1.04	2.35	23.73	0.03	0.02	0.01	0.01	0.01	99.51	2.00	0.00	0.65	0.03	0.14	1.02	3.65	14.55	68.70
	AVG	50.07	0.02	0.04	0.04	21.63	1.19	3.31	24.02	0.06	0.02	0.02	0.03	0.01	100.42	2.00	0.01	0.72	0.04	0.20	1.03	4.19	20.51	75.31
590-26 (N = 5)	MAX	51.32	0.06	0.32	1.06	21.74	0.42	6.54	24.02	0.17	0.01	0.04	0.02	0.04	101.10	2.01	0.10	0.71	0.01	0.39	1.02	1.48	37.57	74.94
	MIN	49.16	0.03	0.07	0.03	18.49	0.29	3.83	23.17	0.06	0.01	0.01	0.02	0.02	99.30	1.96	0.00	0.53	0.01	0.23	0.97	1.02	23.58	61.29
	AVG	50.03	0.05	0.20	0.38	19.89	0.34	5.20	23.69	0.11	0.01	0.03	0.02	0.03	99.90	1.99	0.03	0.63	0.01	0.31	1.01	1.17	31.35	67.48
530-6 (N = 4)	MAX	49.62	0.02	0.57	0.08	28.16	0.63	3.03	23.27	0.10	0.01	0.00	0.27	0.03	100.55	2.01	0.11	0.86	0.02	0.18	1.03	2.26	19.27	95.54
	MIN	47.28	0.01	0.08	0.02	21.95	0.51	0.44	23.08	0.04	0.01	0.00	0.12	0.02	99.12	1.95	0.00	0.75	0.02	0.03	1.00	1.78	2.69	78.47
	AVG	48.73	0.02	0.30	0.05	25.18	0.55	1.66	23.19	0.07	0.01	0.00	0.20	0.02	99.85	1.99	0.03	0.83	0.02	0.10	1.02	1.95	10.38	87.67
530-14 (N = 5)	MAX	50.08	0.02	0.68	0.07	25.61	0.61	4.00	24.16	0.13	0.06	0.06	0.15	0.02	100.88	2.02	0.06	0.87	0.02	0.24	1.03	2.14	24.68	91.42
	MIN	48.50	0.01	0.14	0.03	21.18	0.34	1.16	23.10	0.08	0.03	0.01	0.02	0.01	99.41	1.98	0.00	0.68	0.01	0.07	1.00	1.23	7.35	73.18
	AVG	49.46	0.02	0.39	0.05	23.74	0.50	2.40	23.51	0.10	0.04	0.04	0.09	0.02	100.33	1.99	0.02	0.78	0.02	0.14	1.02	1.79	14.94	83.27
LM-7X (N = 4)	MAX	49.71	0.02	0.21	0.07	24.41	1.24	2.25	23.76	0.25	0.05	0.04	0.04	0.02	100.67	2.01	0.04	0.82	0.04	0.14	1.04	4.51	14.22	86.61
	MIN	48.79	0.01	0.09	0.05	23.25	0.99	1.39	23.36	0.07	0.04	0.03	0.04	0.02	99.52	1.99	0.00	0.76	0.03	0.08	1.02	3.52	8.88	82.04
	AVG	49.11	0.02	0.16	0.06	23.96	1.09	1.81	23.53	0.17	0.05	0.03	0.04	0.02	100.01	2.00	0.02	0.79	0.04	0.11	1.03	3.94	11.39	84.68

Table 2. Cont.

Sample		SiO ₂	TiO ₂	Al ₂ O ₃	Cr ₂ O ₃	FeO	MnO	MgO	CaO	Na ₂ O	K ₂ O	NiO	SnO ₂	P ₂ O ₅	Total	Si	Fe ³⁺	Fe ²⁺	Mn	Mg	Ca	Jo	Di	Hd
LM-14X (N = 3)	MAX	50.87	0.02	0.36	0.09	21.73	0.40	6.30	24.36	0.13	0.01	0.02	0.10	0.04	100.89	2.01	0.07	0.72	0.01	0.37	1.04	1.39	38.28	74.04
	MIN	49.18	0.02	0.07	0.04	17.98	0.23	4.07	23.57	0.07	0.01	0.01	0.02	0.01	98.86	1.97	0.00	0.52	0.01	0.24	1.00	0.81	24.65	60.91
	AVG	49.81	0.02	0.20	0.07	20.04	0.34	5.10	23.93	0.11	0.01	0.02	0.06	0.03	99.67	1.99	0.04	0.62	0.01	0.30	1.02	1.17	30.89	67.94
LM-21X (N = 4)	MAX	50.38	0.02	0.11	0.06	21.90	1.03	5.16	24.58	0.09	0.02	0.06	0.01	0.02	100.45	2.01	0.02	0.73	0.03	0.31	1.05	3.65	31.78	76.71
	MIN	49.82	0.01	0.05	0.01	18.76	0.48	3.14	23.37	0.05	0.02	0.03	0.01	0.01	99.22	1.99	0.00	0.60	0.02	0.19	1.00	1.65	19.64	64.70
	AVG	50.05	0.01	0.08	0.03	20.30	0.84	4.25	24.10	0.07	0.02	0.05	0.01	0.02	99.76	2.00	0.01	0.67	0.03	0.25	1.03	2.97	26.35	70.68
LM-22X (N = 4)	MAX	50.78	0.02	0.09	0.06	23.21	1.69	5.07	24.19	0.08	0.00	0.06	0.01	0.03	100.85	2.01	0.07	0.77	0.06	0.30	1.03	5.68	31.11	80.72
	MIN	49.00	0.01	0.08	0.05	19.21	0.76	2.58	23.62	0.06	0.00	0.01	0.01	0.02	99.45	1.97	0.00	0.60	0.03	0.15	1.02	2.65	16.01	66.24
	AVG	49.89	0.01	0.09	0.06	20.87	1.10	4.19	23.95	0.07	0.00	0.04	0.01	0.02	100.02	2.00	0.02	0.67	0.04	0.25	1.03	3.80	25.51	70.69

Number of ions based on 6 oxygen atoms. Jo—johannsenite, Di—diopside, Hd—hedenbergite.

Table 3. Major element compositions (wt%) of the wollastonite.

Sample		SiO ₂	Al ₂ O ₃	Cr ₂ O ₃	FeO	MnO	MgO	CaO	Na ₂ O	K ₂ O	NiO	SnO ₂	P ₂ O ₅	Total	Si	Ca	Wo	En	Fs	Ac
1511-2 (N = 4)	MAX	51.53	0.00	0.05	0.10	0.02	0.03	49.62	0.05	0.03	0.01	0.04	0.04	101.46	1.98	2.04	99.68	0.09	0.19	0.19
	MIN	50.79	0.00	0.03	0.10	0.01	0.01	48.83	0.03	0.03	0.01	0.02	0.03	99.91	1.97	2.04	99.56	0.03	0.17	0.12
	AVG	51.17	0.00	0.04	0.10	0.01	0.02	49.27	0.05	0.03	0.01	0.03	0.03	100.74	1.98	2.04	99.60	0.07	0.18	0.17
1511-6 (N = 5)	MAX	51.47	0.02	0.06	0.13	0.03	0.08	47.96	0.06	0.03	0.76	0.06	0.04	99.77	2.00	2.02	99.66	0.23	0.23	0.23
	MIN	50.26	0.01	0.04	0.07	0.01	0.03	47.36	0.01	0.01	0.23	0.01	0.02	98.84	1.99	1.99	99.35	0.09	0.16	0.05
	AVG	50.69	0.01	0.05	0.10	0.02	0.05	47.68	0.03	0.02	0.57	0.03	0.03	99.27	1.99	2.01	99.53	0.15	0.19	0.13
1520-870.3 (N = 6)	MAX	51.60	0.01	0.06	0.18	0.03	0.09	49.73	0.09	0.01	0.06	0.06	0.04	101.68	1.98	2.06	99.61	0.25	0.33	0.33
	MIN	50.41	0.01	0.02	0.07	0.01	0.01	48.34	0.03	0.01	0.01	0.01	0.02	99.02	1.96	2.03	99.42	0.04	0.12	0.00
	AVG	51.04	0.01	0.04	0.11	0.02	0.04	49.24	0.06	0.01	0.02	0.03	0.03	100.61	1.98	2.04	99.52	0.10	0.19	0.19
1520-870.9 (N = 5)	MAX	51.92	0.00	0.05	0.27	0.03	0.09	49.23	0.18	0.02	2.19	0.03	0.05	101.62	2.01	2.05	99.48	0.26	0.43	0.70
	MIN	49.96	0.00	0.02	0.07	0.01	0.06	46.32	0.01	0.02	0.01	0.01	0.01	98.98	1.97	1.96	99.07	0.18	0.05	0.00
	AVG	50.92	0.00	0.03	0.21	0.02	0.08	48.27	0.08	0.02	0.56	0.02	0.03	100.02	1.98	2.02	99.30	0.24	0.28	0.18
530-8 (N = 5)	MAX	51.55	0.01	0.05	0.09	0.04	0.06	49.98	0.11	0.03	0.07	0.06	0.04	101.66	1.97	2.05	99.84	0.17	0.20	0.40
	MIN	49.83	0.01	0.03	0.02	0.01	0.02	48.53	0.01	0.01	0.01	0.01	0.01	98.67	1.97	2.04	99.23	0.06	0.04	0.00
	AVG	50.51	0.01	0.04	0.06	0.03	0.05	48.97	0.05	0.02	0.04	0.04	0.02	99.76	1.97	2.05	99.61	0.13	0.11	0.14
530-9 (N = 4)	MAX	51.50	0.05	0.07	0.14	0.00	0.11	49.81	0.07	0.02	0.13	0.04	0.06	101.56	1.99	2.06	99.72	0.32	0.22	0.26
	MIN	49.71	0.01	0.02	0.03	0.00	0.01	48.15	0.01	0.01	0.09	0.02	0.02	98.25	1.97	2.01	99.38	0.03	0.04	0.04
	AVG	50.61	0.03	0.04	0.07	0.00	0.07	48.76	0.04	0.02	0.11	0.03	0.03	99.70	1.98	2.04	99.56	0.21	0.11	0.13

Table 3. Cont.

Sample		SiO ₂	Al ₂ O ₃	Cr ₂ O ₃	FeO	MnO	MgO	CaO	Na ₂ O	K ₂ O	NiO	SnO ₂	P ₂ O ₅	Total	Si	Ca	Wo	En	Fs	Ac
530-14 (N = 5)	MAX	51.52	0.01	0.05	0.26	0.03	0.08	48.30	0.06	0.02	0.02	0.00	0.04	99.27	2.01	2.03	99.72	0.23	0.44	0.22
	MIN	50.46	0.01	0.04	0.08	0.01	0.03	47.35	0.01	0.01	0.01	0.00	0.01	98.42	1.98	1.97	99.29	0.09	0.18	0.00
	AVG	50.91	0.01	0.03	0.14	0.02	0.06	47.82	0.03	0.02	0.02	0.00	0.03	99.01	1.99	2.01	99.51	0.16	0.24	0.09
590-27 (N = 5)	MAX	51.32	0.02	0.07	0.12	0.02	0.07	47.65	0.04	0.02	0.84	0.04	0.03	99.52	2.00	2.01	99.59	0.20	0.22	0.16
	MIN	50.21	0.01	0.01	0.09	0.01	0.04	47.12	0.01	0.01	0.31	0.01	0.02	98.22	1.99	1.99	99.47	0.12	0.17	0.05
	AVG	50.58	0.02	0.04	0.11	0.02	0.06	47.45	0.03	0.02	0.61	0.03	0.02	98.95	1.99	2.00	99.53	0.16	0.20	0.11

Number of ions based on 6 oxygen atoms. Wo—wollastonite, En—enstatite, Fs—Ferrosilite, Ac—aegirine.

5.1.5. Axinite

Axinite is a hydrated silicate mineral of the retrograde skarn stage, with reddish brown and euhedral grains. Axinite coexists mainly with carbonates and is one of the end products of the skarn stage. It cuts and replaces garnet, pyroxene, and epidote. Axinite is intimately related to ore minerals produced by the ore-forming fluids; arsenopyrite and sphalerite can be seen coexisting with it in the axinite hornfels. Therefore, the axinite is formed during the late stage of skarnization and the early stage of mineralization, which is a transitional period. Under plane-polarized light, the axinite is wedge-shaped or plate-prismatic (Figure 6m–o), colorless or pale yellow, and interference colors not exceeding yellow, sometimes with weak abnormal interference colors.

The EPMA results for axinite are listed in Table 4, with SiO₂ contents ranging from 41.59 to 43.29 wt% (avg. 42.33 wt%), Al₂O₃ contents ranging from 16.42 to 18.25 wt% (avg. 17.39 wt%), CaO contents ranging from 18.49 to 20.17 wt% (avg. 19.60 wt%), FeO contents ranging from 5.01 to 9.99 wt% (avg. 7.64 wt%), MnO contents ranging from 1.31 to 7.64 wt% (avg. 4.48 wt%), and B₂O₃ contents ranging from 5.98 to 6.19 wt% (avg. 6.10 wt%, B₂O₃ content calculated based on 32(O, OH) cation). The axinite in the Dachang ore field is mainly ferroaxinite (Figure 7b).

5.1.6. Actinolite

Actinolite is a common mineral of the retrograde skarn stage and is an important hydrated silicate mineral in the Dachang ore field. It often coexists with hydrated silicate minerals such as chlorite and epidote and metasomatized prograde skarn rocks and is closely related to mineralization. Under plane-polarized light, it appeared as a green fibrous and radiated aggregate (Figure 6q,r) with significant pleochromism and interference color ranging from the top of level I to the middle of level II.

The EPMA results for actinolite are listed in Table 5, with the SiO₂ content ranging from 49.05 to 55.92 wt% (avg. 51.53 wt%); the TFeO content ranging from 23.27 to 28.66 wt% (avg. 26.41 wt%); the CaO content ranging from 10.16 to 12.93 wt% (avg. 11.83 wt%); the MgO content ranging from 4.67 to 7.11 wt% (avg. 5.59 wt%); the Al₂O₃ content ranging from 1.77 to 3.59 wt% (avg. 2.40 wt%). The contents of TiO₂, MnO, Na₂O, K₂O, and Cr₂O₅ are relatively low, and a small amount of SnO₂ (0 to 0.10 wt%) is also detected in the actinolite. The Mg/(Mg + Fe²⁺) ratio of the actinolite ranged from 0.23 to 0.34, indicating that it was mainly an Fe-actinolite (Figure 7e).

5.1.7. Epidote

Retrograde skarn stage minerals such as epidote and actinolite are replaced by anhydrous silicate minerals formed during the prograde skarn stage and are intimately related to mineralization. The epidote occurs as small and mostly irregular grains between the garnet, pyroxene, and vesuvianite (Figure 6p). Under plane-polarized light, the epidote is green to yellow-green granular and columnar shaped with bright but uneven interference colors.

The EPMA results showed that the main element components of the epidote are SiO₂, Al₂O₃, CaO, and FeO (Table 6), with SiO₂ contents ranging from 36.15 to 39.09 wt% (avg. 37.65 wt%); Al₂O₃ contents ranging from 20.91 to 25.12 wt% (avg. 22.93 wt%); CaO contents ranging from 23.17 to 24.85 wt% (avg. 23.91 wt%); and TFeO contents ranging from 9.57 to 12.55 wt% (avg. 11.26 wt%). The contents of MgO, TiO₂, MnO, Na₂O, K₂O, and Cr₂O₅ are relatively low. A small amount of SnO₂ (0 to 0.05 wt%) is also detected in the epidote.

5.2. LA-ICP-MS Analysis Results

In this study, prograde skarn rock garnet and retrograde skarn rock axinite were selected for LA-ICP-MS trace element analysis.

5.2.1. Garnet

The trace element analysis results for garnet were published by He et al. [24]. The results showed that both generations of garnets are depleted in large ion lithophile elements

(LILEs) such as Rb, Cs, Ba, and K compared to the primitive mantle [35]. The Hf content ranges from 0.62 to 2.48 ppm; Zr ranges from 15.54 to 101.13 ppm; Nb ranges from 0.45 to 7.96 ppm; Ta ranges from 0.02 to 0.83 ppm; Th ranges from 0 to 0.76 ppm; and U ranges from 0 to 0.84 ppm.

All garnets contain ore-forming elements such as W, Sn, As, In, Ge, and Ga, and apart from Ga, the content of other ore-forming elements is lower in Grt I than in Grt II. The W content ranges from 0.17 to 12.8 ppm; Sn ranges from 340 to 4137 ppm; As ranges from 0 to 6.3 ppm; In ranges from 1.8 to 46.8 ppm; Ge ranges from 2.6 to 23.6 ppm; and Ga ranges from 20.3 to 43.0 ppm.

All garnets show characteristics of heavy rare earth element (HREE) enrichment and light rare earth element depletion (LREE; Figure 8), compared to the chondrite. The total rare earth element (Σ REE) content varies from 6.02 to 59.30 ppm; the Σ LREE/ Σ HREE ratio varies from 0.01 to 0.67, with obvious negative to slightly negative Eu anomalies (δ Eu = 0.18–0.94). The Σ REE content and the Σ LREE/ Σ HREE ratio are lower in Grt I than in Grt II, while δ Eu is higher than in Grt II.

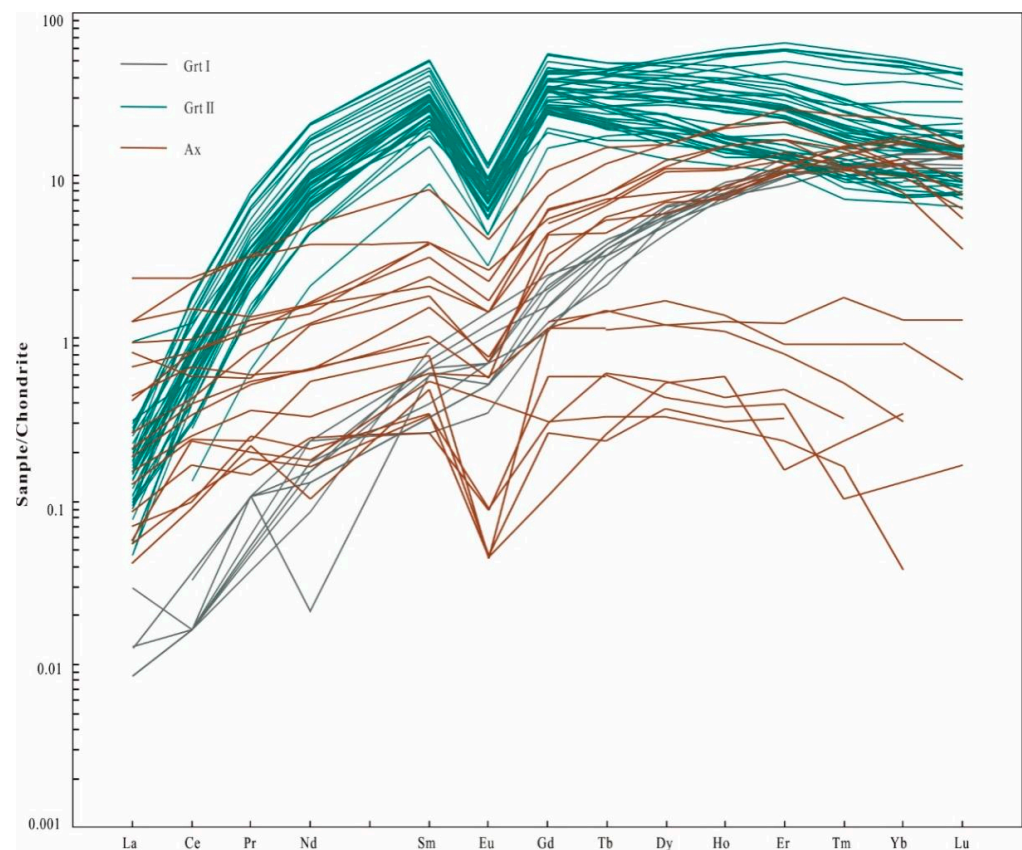


Figure 8. Chondrite-normalized REE patterns of garnets and axinites (normalization values after [35]).

5.2.2. Axinite

The trace element contents of the axinite are listed in Table 7. The Σ REE content of sample 1511-20-4 is 200.42 ppm, which is significantly higher than that of other axinites. It is speculated that this analysis point may contain REE-rich mineral inclusions and will not be discussed further. Axinite is depleted in LILEs compared to the primitive mantle [36], with contents of elements such as Rb, Cs, Ba, and K below detection limits. The axinite contains 12.2–33.6 ppm Sr, 0–2.4 ppm Nb, and 0.08–39.4 ppm Zr.

Table 4. Major element compositions (wt%) of the axinite.

Sample		SiO ₂	Al ₂ O ₃	TiO ₂	SnO ₂	K ₂ O	CaO	Na ₂ O	MgO	FeO	MnO	Cr ₂ O ₃	H ₂ O *	B ₂ O ₃ *	Total	Si	Al	Ca	Mg	Fe	Mn	OH	B
1511-5-1 (N = 5)	MAX	42.47	17.86	0.08	0.00	0.00	20.01	0.02	0.41	9.53	5.23	0.06	1.51	6.16	101.30	8.04	3.96	4.05	0.12	1.51	0.83	2.00	2.00
	MIN	42.04	16.93	0.01	0.00	0.00	19.62	0.01	0.09	8.13	3.86	0.02	1.48	6.07	99.70	7.97	3.79	4.00	0.02	1.28	0.62	2.00	2.00
	AVG	42.24	17.39	0.05	0.00	0.00	19.84	0.02	0.24	8.58	4.48	0.04	1.50	6.12	100.40	8.00	3.88	4.03	0.07	1.36	0.72	2.00	2.00
1511-5-2 (N = 5)	MAX	42.43	17.64	0.10	0.15	0.03	20.17	0.00	0.86	9.99	4.84	0.11	1.50	6.13	100.40	8.04	3.93	4.08	0.24	1.58	0.78	2.00	2.00
	MIN	41.86	16.65	0.01	0.03	0.03	19.39	0.00	0.05	7.51	2.75	0.03	1.47	6.03	99.00	7.97	3.77	3.95	0.02	1.19	0.44	2.00	2.00
	AVG	42.16	17.27	0.05	0.08	0.03	19.67	0.00	0.58	8.74	3.77	0.07	1.49	6.10	99.98	8.01	3.87	4.00	0.17	1.39	0.61	2.00	2.00
1511-3-1 (N = 8)	MAX	42.44	17.52	0.07	0.13	0.03	19.73	0.02	0.45	9.66	6.09	0.10	1.49	6.09	100.30	8.10	3.93	4.06	0.13	1.56	0.98	2.00	2.00
	MIN	41.59	16.42	0.02	0.06	0.01	19.06	0.01	0.28	5.63	3.77	0.01	1.46	5.98	98.00	7.96	3.74	3.96	0.08	0.90	0.61	2.00	2.00
	AVG	41.96	16.95	0.05	0.09	0.01	19.48	0.02	0.36	8.12	4.61	0.05	1.48	6.04	99.15	8.04	3.83	4.00	0.10	1.30	0.75	2.00	2.00
1511-3-2 (N = 7)	MAX	42.53	17.72	0.00	0.03	0.02	19.91	0.02	0.43	8.91	6.62	0.06	1.50	6.14	100.30	8.07	3.94	4.07	0.12	1.42	1.06	2.00	2.00
	MIN	41.93	17.22	0.00	0.01	0.01	19.51	0.01	0.37	5.43	3.78	0.02	1.48	6.05	98.70	8.00	3.85	4.00	0.11	0.87	0.61	2.00	2.00
	AVG	42.22	17.33	0.00	0.02	0.01	19.75	0.01	0.39	7.30	5.12	0.04	1.49	6.09	99.76	8.03	3.88	4.02	0.11	1.16	0.83	2.00	2.00
1511-3-3 (N = 8)	MAX	42.82	17.67	0.09	0.07	0.02	19.89	0.02	0.53	9.83	6.37	0.21	1.50	6.15	100.80	8.10	3.94	4.04	0.15	1.57	1.02	2.00	2.00
	MIN	41.89	16.77	0.02	0.04	0.01	19.26	0.01	0.24	5.72	3.57	0.02	1.48	6.07	99.50	7.99	3.76	3.89	0.07	0.91	0.58	2.00	2.00
	AVG	42.41	17.28	0.04	0.06	0.01	19.57	0.02	0.40	8.01	4.58	0.11	1.49	6.10	99.90	8.05	3.86	3.98	0.11	1.27	0.74	2.00	2.00
1511-20-1 (N = 4)	MAX	42.73	18.09	0.03	0.03	0.03	20.05	0.01	1.29	8.95	7.64	0.02	1.51	6.18	100.10	8.06	4.00	4.03	0.36	1.40	1.23	2.00	2.00
	MIN	42.07	17.44	0.01	0.03	0.01	18.49	0.01	0.56	5.01	1.31	0.02	1.48	6.08	99.20	8.01	3.92	3.76	0.16	0.79	0.21	2.00	2.00
	AVG	42.44	17.79	0.02	0.03	0.02	19.46	0.01	0.92	7.08	4.20	0.02	1.50	6.13	99.55	8.03	3.97	3.95	0.26	1.12	0.68	2.00	2.00
1511-20-2 (N = 7)	MAX	43.29	18.25	0.04	0.07	0.02	19.81	0.02	1.69	6.58	6.25	0.06	1.51	6.19	100.20	8.10	4.04	3.99	0.47	1.03	1.01	2.00	2.00
	MIN	42.57	17.56	0.01	0.01	0.01	19.24	0.01	0.55	5.25	3.50	0.02	1.49	6.09	99.00	8.00	3.93	3.87	0.16	0.83	0.56	2.00	2.00
	AVG	42.86	17.95	0.03	0.03	0.02	19.45	0.01	1.50	5.87	4.26	0.04	1.51	6.17	99.61	8.05	3.97	3.91	0.42	0.92	0.68	2.00	2.00

* H₂O and B₂O₃ content and number of ions based on 32(O, OH) cation.**Table 5.** Major element compositions (wt%) of the actinolite.

Sample		SiO ₂	TiO ₂	Al ₂ O ₃	Cr ₂ O ₃	FeO	MnO	MgO	CaO	Na ₂ O	K ₂ O	NiO	SnO ₂	P ₂ O ₅	Total	Si	Al	Cr	Fe	Mn	Mg	Ca	Na	K
LM-4X (N = 3)	MAX	55.92	0.04	2.19	1.76	26.59	0.87	5.13	11.54	0.21	0.13	0.05	0.10	0.00	99.67	8.23	0.38	0.20	3.31	0.11	1.13	1.83	0.06	0.02
	MIN	54.51	0.01	1.77	0.02	23.27	0.42	4.67	10.16	0.17	0.11	0.00	0.00	0.00	99.38	8.08	0.31	0.00	2.86	0.05	1.04	1.60	0.05	0.02
	AVG	55.11	0.02	1.97	0.89	24.79	0.72	4.94	10.67	0.19	0.12	0.03	0.06	0.00	99.51	8.17	0.34	0.10	3.07	0.09	1.09	1.69	0.05	0.02
LM-5X (N = 3)	MAX	52.64	0.06	2.48	1.37	28.66	1.07	5.52	12.37	0.28	0.21	0.06	0.07	0.01	101.58	7.85	0.44	0.16	3.58	0.14	1.24	2.00	0.08	0.04
	MIN	51.11	0.05	1.95	0.14	26.31	0.60	4.83	11.64	0.18	0.18	0.00	0.00	0.00	100.36	7.69	0.34	0.02	3.32	0.08	1.07	1.88	0.05	0.03
	AVG	51.72	0.05	2.17	0.82	27.61	0.79	5.21	12.06	0.24	0.19	0.02	0.02	0.01	100.91	7.76	0.38	0.10	3.47	0.10	1.17	1.94	0.07	0.04
LM-17X (N = 3)	MAX	50.49	0.05	3.59	0.93	28.49	0.92	5.38	12.44	0.24	0.26	0.06	0.02	0.03	100.12	7.68	0.64	0.11	3.62	0.12	1.23	2.03	0.07	0.05
	MIN	49.87	0.02	2.42	0.09	26.80	0.67	5.07	11.82	0.15	0.17	0.00	0.00	0.00	98.83	7.63	0.44	0.01	3.41	0.09	1.15	1.95	0.04	0.03
	AVG	50.17	0.03	2.89	0.38	27.49	0.78	5.23	12.08	0.20	0.20	0.03	0.01	0.01	99.50	7.66	0.52	0.04	3.51	0.10	1.19	1.98	0.06	0.04
LM-22X (N = 3)	MAX	50.10	0.08	3.51	0.62	26.61	0.90	6.24	12.93	0.24	0.26	0.01	0.05	0.01	98.54	7.69	0.64	0.08	3.41	0.12	1.43	2.14	0.07	0.05
	MIN	49.05	0.03	2.38	0.12	25.89	0.57	4.97	12.00	0.15	0.23	0.00	0.03	0.00	98.21	7.57	0.43	0.01	3.34	0.07	1.14	1.97	0.04	0.04
	AVG	49.55	0.06	2.88	0.29	26.28	0.71	5.78	12.31	0.20	0.24	0.01	0.04	0.01	98.36	7.63	0.52	0.03	3.38	0.09	1.32	2.03	0.06	0.05

Table 5. Cont.

Sample		SiO ₂	TiO ₂	Al ₂ O ₃	Cr ₂ O ₃	FeO	MnO	MgO	CaO	Na ₂ O	K ₂ O	NiO	SnO ₂	P ₂ O ₅	Total	Si	Al	Cr	Fe	Mn	Mg	Ca	Na	K
1511-1 (N = 3)	MAX	51.84	0.04	2.28	0.86	27.66	0.87	7.11	12.21	0.23	0.17	0.01	0.00	0.02	100.25	7.76	0.40	0.10	3.55	0.11	1.59	1.96	0.07	0.03
	MIN	50.47	0.04	1.99	0.06	24.76	0.73	5.72	11.58	0.16	0.15	0.00	0.00	0.00	98.77	7.72	0.36	0.01	3.10	0.09	1.31	1.91	0.05	0.03
	AVG	50.99	0.04	2.13	0.41	26.15	0.80	6.41	11.90	0.19	0.16	0.00	0.00	0.01	99.20	7.74	0.38	0.05	3.32	0.10	1.45	1.94	0.06	0.03

Number of ions based on 23 oxygen atoms.

Table 6. Major element compositions (wt%) of the epidote.

Sample		SiO ₂	TiO ₂	Al ₂ O ₃	Cr ₂ O ₃	FeO	MnO	MgO	CaO	Na ₂ O	K ₂ O	NiO	SnO ₂	P ₂ O ₅	Total	Si	Al	Fe	Ca	H	Ep
1511-7 (N = 4)	MAX	39.09	0.11	25.12	0.06	10.33	0.25	0.04	24.85	0.00	0.01	0.04	0.03	0.05	97.39	3.18	2.42	0.70	2.16	1.00	23.30
	MIN	37.45	0.01	22.85	0.02	9.57	0.16	0.00	23.65	0.00	0.00	0.00	0.00	0.00	95.79	3.06	2.19	0.65	2.07	1.00	21.28
	AVG	38.17	0.06	23.97	0.04	9.95	0.18	0.02	24.12	0.00	0.01	0.02	0.01	0.02	96.56	3.12	2.31	0.68	2.11	1.00	22.77
1511-10 (N = 4)	MAX	37.28	0.12	22.98	1.06	12.55	0.14	0.03	24.35	0.03	0.01	0.04	0.05	0.07	96.54	3.12	2.27	0.88	2.20	1.00	29.87
	MIN	36.15	0.00	20.91	0.26	11.12	0.04	0.00	23.17	0.00	0.00	0.02	0.00	0.00	95.32	3.03	2.07	0.78	2.08	1.00	25.80
	AVG	36.76	0.04	22.07	0.65	12.08	0.09	0.02	23.89	0.01	0.00	0.03	0.03	0.03	95.70	3.08	2.18	0.85	2.15	1.00	28.00
590-21 (N = 3)	MAX	38.44	0.08	22.84	0.04	12.07	0.22	0.06	23.84	0.02	0.01	0.09	0.05	0.03	97.53	3.14	2.20	0.82	2.08	1.00	27.35
	MIN	37.74	0.05	22.53	0.03	11.83	0.19	0.05	23.47	0.00	0.00	0.00	0.00	0.01	96.15	3.13	2.19	0.81	2.08	1.00	26.88
	AVG	38.14	0.07	22.70	0.04	11.92	0.20	0.05	23.68	0.01	0.01	0.05	0.03	0.02	96.91	3.13	2.20	0.82	2.08	1.00	27.14

Number of ions based on 12.5 oxygen atoms. Ep = clinozoisite component in epidote ($\text{Fe}^{3+}/(\text{Fe}^{3+} + \text{Al}^{\text{VI}}) \times 100$).

Table 7. Trace element compositions (ppm) of the axinite.

Sample		Be	P	Sc	Ti	V	Cr	Ga	Ge	As	Sr	Zr	Nb	Mo	In	Sn	Sb	Cs	Ba	La	Ce	Pr	Nd
1511-3 (N = 8)	MAX	26.9	268	10.4	24.8	319	84.4	28.3	3.7	8.9	14.6	2.0	0.01	0.29	0.88	162	0.56	0.11	3.8	0.05	0.21	0.05	0.31
	MIN	4.4	220	1.3	12.5	220	21.0	16.9	2.8	0.82	12.2	0.08	0.01	0.17	0.30	31.6	0.16	0.05	0.04	0.01	0.06	0.01	0.05
	AVG	14.8	244	6.2	17.6	296	58.0	20.3	3.3	3.2	13.7	0.77	0.01	0.25	0.48	64.8	0.24	0.08	1.9	0.02	0.12	0.02	0.15
1511-20 (N = 11)	MAX	43.4	1066	7.4	151	186	168	17.3	8.4	3.4	33.6	39.4	2.4	0.33	8.9	776	0.88	2.0	3.2	0.56	1.46	0.30	2.33
	MIN	1.3	271	0.54	58.9	109	5.9	11.0	5.3	1.2	15.6	6.6	0.04	0.11	3.0	162	0.13	0.13	0.03	0.05	0.24	0.05	0.30
	AVG	18.6	380	2.9	92.3	142	61.6	13.2	6.6	2.7	21.9	18.6	0.54	0.26	5.7	413	0.48	1.0	0.66	0.21	0.66	0.13	0.88

Table 7. Cont.

Sample		Sm	Eu	Gd	Tb	Dy	Ho	Er	Tm	Yb	Lu	Y	Hf	Ta	W	Pb	Th	U	ΣREE	LREE/HREE	LaN/YbN	δEu	δCe
1511-3 (N = 8)	MAX	0.14	0.03	0.26	0.06	0.44	0.08	0.20	0.05	0.22	0.03	2.21	0.11	0.00	0.01	0.09	0.01	0.01	1.94	1.54	3.39	0.70	2.20
	MIN	0.04	0.01	0.05	0.01	0.09	0.02	0.03	0.01	0.01	0.01	0.45	0.01	0.00	0.01	0.05	0.01	0.01	0.44	0.43	0.00	0.00	0.74
	AVG	0.08	0.02	0.15	0.03	0.20	0.04	0.09	0.02	0.10	0.02	1.10	0.00	0.00	0.01	0.07	0.01	0.01	0.98	0.84	0.98	0.15	1.24
1511-20 (N = 11)	MAX	1.26	0.23	2.22	0.55	3.94	1.13	4.27	0.59	3.76	0.38	40.40	1.15	0.01	0.11	0.85	0.69	0.22	19.55	0.59	0.19	0.57	1.31
	MIN	0.16	0.03	0.58	0.17	1.48	0.41	1.70	0.27	1.33	0.09	15.10	0.18	0.01	0.01	0.20	0.02	0.01	9.39	0.10	0.01	0.27	0.86
	AVG	0.49	0.10	1.16	0.29	2.64	0.70	2.48	0.36	2.32	0.24	24.62	0.51	0.01	0.06	0.45	0.20	0.12	12.64	0.24	0.07	0.39	1.04

The axinite contains ore-forming elements such as Sn, As, In, Ge, and Ga. The content of Sn in the axinite ranges from 31.6 to 706 ppm, As ranges from 0.82 to 8.9 ppm, Ge ranges from 2.8 to 8.4 ppm, Ga ranges from 11.0 to 28.3 ppm, and In ranges from 0.30 to 8.9 ppm.

The chondrite-normalized REE pattern of the axinite shows a significant fractionation of light and heavy rare earth elements (Figure 8), with $\Sigma\text{LREE}/\Sigma\text{HREE}$ ratios ranging from 0.10 to 0.97 (with a point value of 1.54) and significantly negative Eu anomalies ($\delta\text{Eu} = 0.00\text{--}0.70$, avg. 0.28). The ΣREE content ranges from 0.44 to 19.55 ppm.

6. Discussion

6.1. Redox Conditions of the Ore-Forming Fluids

Different redox conditions often produce different skarn rocks, so the mineral assemblages and chemical compositions of skarn rocks can be used to constrain the redox conditions of the ore-forming fluids [3,4,36–39]. The contents and chemical compositions of garnet have significant implications for the redox conditions of ore-forming fluids [3,39]. When the oxygen fugacity of the fluid was high, the skarn rocks had a relatively high $\text{Fe}^{3+}/\text{Fe}^{2+}$ ratio, and andradite was formed. However, when the oxygen fugacity of the fluid was low, the skarn rocks had a relatively high $\text{Fe}^{2+}/\text{Fe}^{3+}$ ratio, and grossular was formed [40–46]. Based on the temperature– $\log f\text{O}_2$ diagram for stable skarn rocks and sulfide assemblages at different stages summarized by Meinert et al. [5], we proposed an evolution process for the redox conditions of ore-forming fluids at the skarn stage.

The earliest mineral formed during the skarn stage of the Dachang ore field was grossular, indicating that the early ore-forming fluid during the skarn stage was relatively reduced [24]; with the evolution of the ore-forming fluid, considerable andradite, pyroxene, and wollastonite were formed, indicating an increase in the oxygen fugacity of the ore-forming fluid in the later stage. In the final skarn stage, garnet and pyroxene were replaced by Fe-actinolite, chlorite, and quartz, indicating that the ore-forming conditions changed from relatively oxidized to reduced (Figure 9). Subsequently, many sulfides precipitated under the relatively reduced conditions [1,5]. The δEu of fluorite coexisting with the Zn–Cu ore bodies is 0.16–0.87 (avg. 0.41, unpublished data), also indicating that the ore-forming fluid is under reducing conditions.

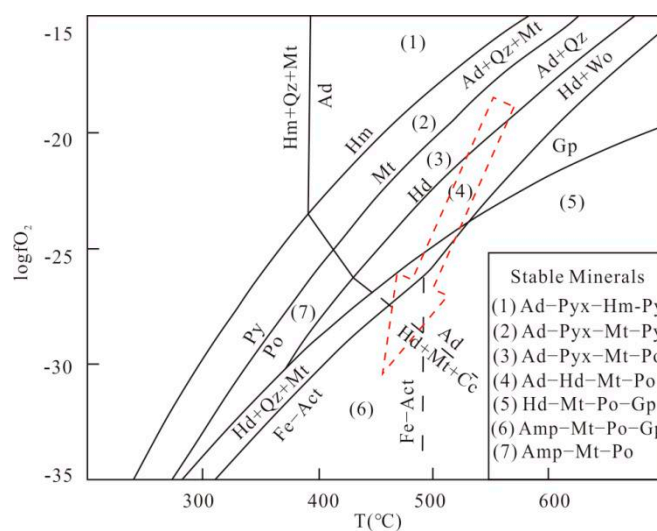


Figure 9. Temperature–log oxygen fugacity diagram, showing the stability fields of major skarn silicate, oxide, and sulfide minerals (Modified from [5]). Mineral abbreviations: Ad = andradite, Amp = amphibole, Cc = calcite, Fe-Act = ferro-actinolite, Gp = graphite, Hd = hedenbergite, Hm = hematite, Mt = magnetite, Po = pyrrhotite, Py = pyrite, Pyx = pyroxene, Qz = quartz, Wo = wollastonite. The red arrow shows the direction of evolution.

6.2. Lithological Control during the Formation of Skarn Rocks

The Zn–Cu ore bodies in the Dachang ore field were intimately related to the retrograde skarn stage. Mineralization mainly occurred in the limestone, black mudstone, and shale of the middle Devonian Luofu Formation (D_2^l) and the limestone of the upper Devonian Wuzhishan Formation (D_3^w). The early generation garnet was mainly composed of grossular; the vesuvianites are Al-rich vesuvianites; the late generation garnet is mainly composed of andradite; the pyroxenes formed a diopside–hedenbergite solid solution; the axinites are mainly ferroaxinites; and the actinolites are Fe-actinolites, indicating that the skarn rocks gradually evolved from early Al-rich to late Fe-rich characteristics. After analyzing the Longxianggai granitic pluton, Liang [6] pointed out that the granitic pluton had a high Al content and was depleted in Fe, indicating that the early ore-forming fluid was mainly composed of magmatic exsolution fluids, and the skarn rocks may mainly reflect the characteristics of the magmatic fluids. After analyzing the geochemistry of the Devonian strata in the Dachang ore field, Han et al. [47] noted that the middle Devonian Luofu Formation (D_2^l) and the upper Devonian Wuzhishan Formation (D_3^w) in this area contained widely distributed spotted, nodular, striped, and banded fine-grained pyrite, and the content of Fe^{2+} was higher than that of Fe^{3+} . The ratio of $Fe^{3+}/(Fe^{3+} + Fe^{2+})$ was typically lower than 0.3%. The late stage of the Fe-rich skarn rocks may indicate that the late ore-forming fluid was strongly influenced by the country rock.

6.3. Implications of Mineralization

EPMA results of the calc-silicates in the Dachang ore field show that all skarn contain a small amount of the ore-forming element Sn. The end-member components of the pyroxene are relatively similar to those of the vast majority of skarn-type Sn deposits worldwide [5]. According to the classification proposed by Sanero and Gottardi [48], the axinite in the Dachang ore field is mainly ferroaxinite (Figure 6b). Qian [49] and Hu et al. [50] analyzed axinite from the Gejiu and Furong Sn deposits and noted that the axinite in these two deposits was also mainly composed of ferroaxinite.

6.3.1. Migration of Ore-Forming Elements during the Evolution of Hydrothermal Fluids

LA-ICP-MS analysis showed that neither the garnet nor the axinite contained Cu, and Zn was not detected in the axinite. We collected the trace element contents of the Longxianggai granitic pluton and the vesuvianite in the Dachang ore field and plotted them (Figure 10). From Longxianggai granitic pluton → garnet → vesuvianite → axinite, the content of ore-forming elements Sn and In first increased and then decreased, with the highest content in garnet; the content of W and As decreased; the content of Zn was relatively low in Longxianggai granitic pluton and garnet, but significantly increased in vesuvianite; and the content of Ga and Ge in skarn rocks did not change significantly.

Sn in garnet is very high; the contents of Sn are 2378 ppm in garnet, 688 ppm in vesuvianite [51] and 281 ppm in axinite. From the prograde skarn stage to the retrograde skarn stage, the Sn content gradually decreased, indicating that the Sn mineralization was not the remobilization of Sn from prograde skarn rocks by hydrothermal fluid. The significant enrichment of Sn in the magmatic hydrothermal fluid is a necessary condition for Sn mineralization. This conclusion is consistent with that drawn by Chen et al. [52] after studying the Furong skarn-type Sn deposit.

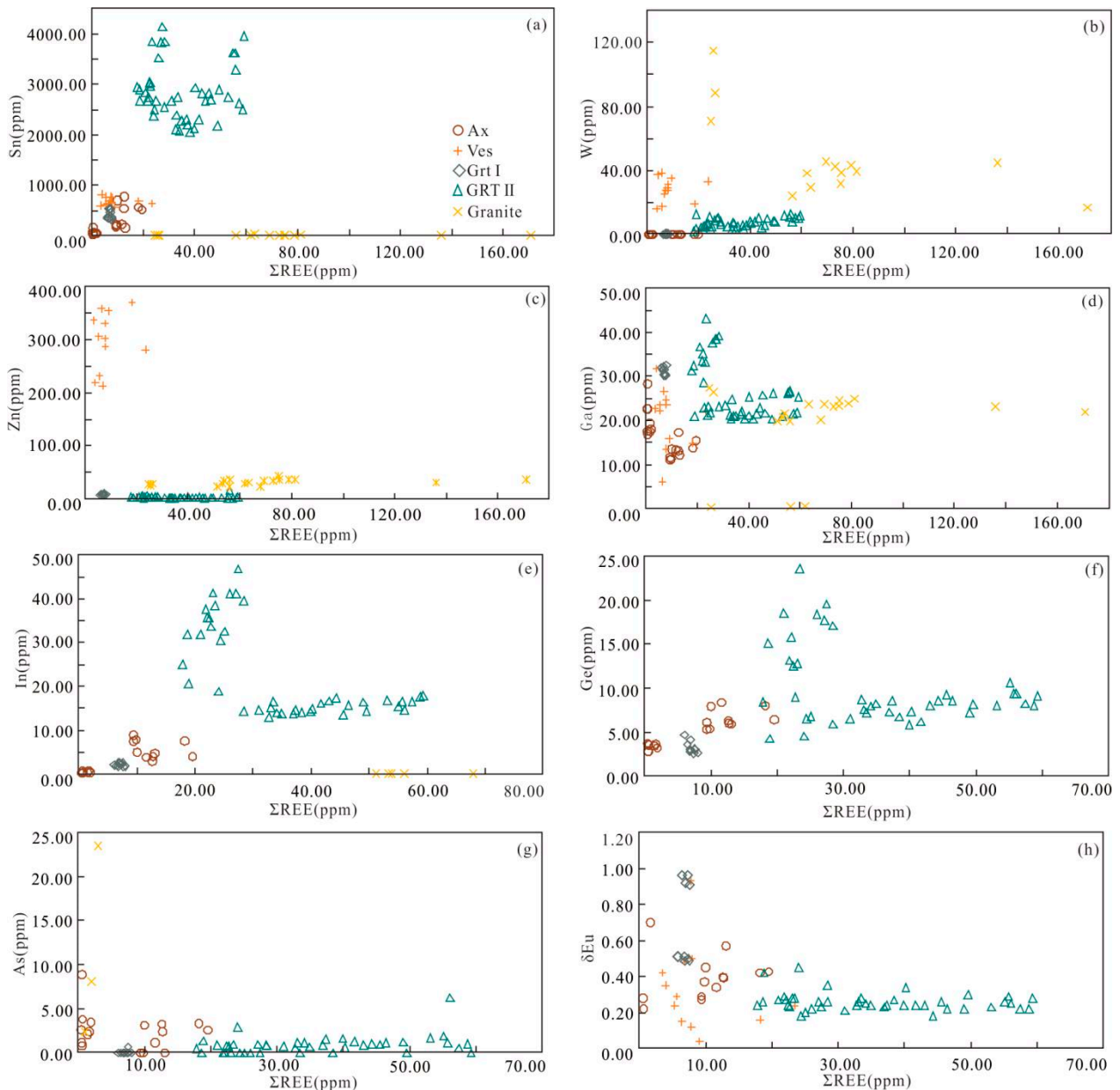


Figure 10. Trace element compositions of skarn rocks and granite by LA-ICP-MS. (Vesuvianite from [48]; granite from [6,11,18]).

6.3.2. Influence of the Volatile on Mineralization

The widely developed minerals such as vesuvianite, axinite, fluorite, and tourmaline in the Dachang ore field indicate that the ore-forming fluid contained large amounts of volatiles F and B. Zhao et al. [53] analyzed the trace elements and B isotopes of tourmaline in the Longxianggai granitic pluton and the Dachang ore field and noted that the ore-forming fluid and volatile B were mainly from magmatic hydrothermal fluids.

Volatiles play a significant role in magma evolution and mineralization. During the partial melting process in the source region, volatiles B and F lowered the solidus temperature of Sn-bearing minerals, facilitating the partial melting of Sn-bearing minerals [54,55]. During magma evolution, the enrichment in B increased the solubility of fluid in the magma system and increased fluid content [56]. F broke the bridging oxygen bonds in the melt, reduced the viscosity of the melt, and to some extent increased the diffusion of the ore-forming elements in the melt, thereby increasing the solubilities of the ore-forming elements in the melt. The presence of volatiles may have prolonged the magma evolution

process and allowed the enrichment of incompatible elements, such as Sn, in the residual magma. During the dissolution of magmatic hydrothermal fluids, volatiles facilitated further enrichment of the ore-forming elements in the hydrothermal fluid and may have formed complexes with $\text{Sn}(\text{BF}_4)_2$ [57], allowing long-distance migration of the ore-forming elements in the hydrothermal fluid [58–62]. The widely distributed volatiles F and B in the ore-forming fluid may be one of the reasons for the large scale of metal deposition and mineralization in the Dachang ore field and also one of the reasons for the formation of Zn–Cu ore bodies proximal to the granitic pluton and Sn polymetallic ore bodies distal to the granitic pluton in the Dachang ore field.

7. Conclusions

(1) Based on the mineral assemblages and chemical composition characteristics of the skarn rocks in the Dachang ore field, the early ore-forming fluid in the skarn stage was in a relatively reduced state; as the ore-forming fluid evolved, the oxygen fugacity of the ore-forming fluid in the later stage increased; in the final skarn stage, the ore-forming conditions changed from a relatively oxidized state to a relatively reduced state, and sulfides were precipitated.

(2) The skarn rocks in the Dachang ore field evolved from early Al-rich to late Fe-rich characteristics, indicating that the early hydrothermal fluids were mainly magmatic exsolution fluids, and the skarn rocks may mainly reflect the characteristics of the magmatic fluids. The late stage of Fe-rich skarn rocks may indicate that the late hydrothermal fluids were strongly influenced by the country rock.

(3) From the prograde skarn stage to the retrograde skarn stage, the Sn content gradually decreased, indicating that the Sn mineralization was not due to the remobilization of Sn from prograde skarn rocks by hydrothermal fluid. The significant enrichment of Sn in the magmatic hydrothermal fluid was a necessary condition for Sn mineralization.

(4) The widely developed minerals such as vesuvianite, axinite, fluorite, and tourmaline in the Dachang ore field indicate that the ore-forming fluid contained large amounts of volatiles F and B. This may be the vital reason for the large-scale mineralization of the Dachang ore field and one of the reasons for the formation of Zn–Cu ore bodies proximal to the granitic pluton and Sn polymetallic ore bodies distal to the granitic pluton in the Dachang ore field.

Author Contributions: Conceptualization, L.H. and T.L.; methodology, L.H.; software, J.Z.; investigation, B.L.; writing—original draft preparation, L.H. and T.L.; writing—review and editing, L.H., T.L. and D.W.; funding acquisition, T.L. All authors have read and agreed to the published version of the manuscript.

Funding: This study is financially supported by the China Geological Survey granted to T. Liang (Grant Number: DD20221695-43, DD20190379).

Data Availability Statement: Data are contained within the article.

Acknowledgments: We would like to thank Minwu Liu and Xijuan Tan from Chang'an University. We also thank the editors and three anonymous reviewers for their editorial handling and constructive comments on this manuscript.

Conflicts of Interest: Author Jianxin Zhang was employed by the company Northwest Bureau of China Metallurgical Geology Bureau, and author Bosheng Liu was employed by the company Guangxi 215 Geological Team Co., Ltd. The remaining authors declare that the research was conducted in the absence of any commercial or financial relationships that could be construed as a potential conflict of interest.

References

1. Leng, Q.F.; Tang, J.X.; Zheng, W.B.; Tang, P.; Lin, B. Skarn mineral assemblage and zonation pattern in the Jiama superlarge deposit, Tibet. *Acta Geol. Sin.* **2022**, *96*, 574–591. (In Chinese with English Abstract)
2. Liu, L.J.; Zhou, T.F.; Fu, B.; Ireland, T.R.; Zhang, D.Y.; Liu, G.X.; Yuan, F.; Zha, X.P.; White, N.C. Multiple fluid sources in skarn systems: Oxygen isotopic evidence from the Haobugao Zn-Fe-Sn deposit in the southern Great Xing'an Range, NE China. *Am. Mineral.* **2023**, *108*, 1957–1972. [[CrossRef](#)]
3. Meinert, L.D. Skarns and skarn deposits. *Geosci. Can.* **1992**, *19*, 145–162.
4. Meinert, L.D.; Hefton, K.K.; Mayes, D.; Tasiran, I. Geology, zonation, and fluid evolution of the Big Gossan Cu-Au skarn deposit, Ertsberg district, Irian Jaya. *Econ. Geol.* **1997**, *92*, 509–534. [[CrossRef](#)]
5. Meinert, L.D.; Dipple, G.; Nicolescu, S. World skarn deposits. *Econ. Geol.* **2005**, *100*, 299–336.
6. Liang, T. Study on the Metallogenic Mechanism of Changpo–Tongkeng Tin-polymetallic Deposit, Dachang, Guangxi. Ph.D. Thesis, Chang'an University, Xi'an, China 2008; pp. 1–260. (In Chinese with English Abstract)
7. Liang, T.; Wang, D.H.; Hou, K.J.; Li, H.Q.; Huang, M.H.; Cai, M.H.; Wang, D.M. LA-MC-ICP-MS zircon U-Pb dating of Longxianggai pluton in Dachang of Guangxi and its geological significance. *Acta Petrol. Sin.* **2011**, *27*, 1624–1636. (In Chinese with English Abstract)
8. Wang, X.Y.; Huang, H.W.; Chen, N.S.; Huang, X.Q.; Wu, X.K.; Hao, S.; Li, H.M. In-situ LA-MC-ICP MS U-Pb Geochronology of Cassiterite from Changpo–Tongkeng Tin-Polymetallic Deposits, Dachang Orefield, Guangxi. *Geol. Review* **2015**, *61*, 892–900. (In Chinese with English Abstract)
9. Wang, D.H.; Chen, Y.C.; Chen, W.; Sang, H.Q.; Li, H.Q.; Lu, Y.F.; Chen, K.L.; Lin, Z.M. Dating the Dachang Giant Tin-Polymetallic Deposit in Nandan, Guangxi. *Acta Geol. Sin.* **2004**, *78*, 132–138. (In Chinese with English Abstract)
10. Huang, W.T.; Liang, H.Y.; Zhang, J.; Wu, J.; Chen, X.L.; Ren, L. Genesis of the Dachang Sn-polymetallic and Baoshan Cu ore deposits, and formation of a Cretaceous Sn-Cu ore belt from southwest China to western Myanmar. *Ore Geol. Rev.* **2019**, *112*, 103030. [[CrossRef](#)]
11. Wang, T.Y.; Li, G.J.; Wang, Q.E.; Santosh, M.; Zhang, Q.Z.; Deng, J. Petrogenesis and metallogenic implications of Late Cretaceous I- and S-type granites in Dachang–Kunlunquan ore belt, southwestern South China Block. *Ore Geol. Rev.* **2019**, *113*, 103079. [[CrossRef](#)]
12. Guo, J.; Zhang, R.Q.; Sun, W.D.; Ling, M.X.; Hu, Y.B.; Wu, K.; Luo, M.; Zhang, L.C. Genesis of tin-dominant polymetallic deposits in the Dachang district, South China: Insights from cassiterite U-Pb ages and trace element compositions. *Ore Geol. Rev.* **2018**, *95*, 863–879. [[CrossRef](#)]
13. Li, H.Q.; Wang, D.H.; Mei, Y.P.; Liang, T.; Chen, Z.Y.; Guo, C.L.; Ying, L.J. Lithogenesis and Mineralization Chronology Study on the Lamo Zinc-Copper Polymetallic Ore Deposit in Dachang Orefield, Guangxi. *Acta Geol. Sin.* **2008**, *82*, 912–920. (In Chinese with English Abstract)
14. Cai, M.H.; He, L.Q.; Liu, G.Q.; Wu, D.C.; Huang, H.M. SHRIMP Zircon U-Pb Dating of the Intrusive Rocks in the Dachang Tin Polymetallic Ore Field, Guangxi and Their Geological Significance. *Geol. Rev.* **2006**, *52*, 409–414. (In Chinese with English Abstract)
15. Chen, Y.C.; Huang, M.Z.; Xu, J.; Hu, Y.Z.; Tang, S.H.; Li, Y.Q.; Meng, L.K. *Geology of Dachang Tin Deposit*; Geological Publishing House: Beijing, China, 1993; pp. 1–361. (In Chinese with English Abstract)
16. Cai, M.H.; Peng, Z.A.; Hu, Z.S.; Li, Y.Z. He-Ar and Sr-Nd isotopic compositions of the Tongkeng Tin-polymetallic ore deposit in south China: Implication for ore genesis. *Ore Geol. Rev.* **2020**, *124*, 1–12. [[CrossRef](#)]
17. Cai, M.H.; Mao, J.W.; Liang, T.; Franco, P.; Huang, H.L. The origin of the Tongkeng–Changpo tin deposit, Dachang metal district, Guangxi, China: Clues from fluid inclusions and He isotope systematics. *Miner. Depos.* **2007**, *42*, 613–626.
18. Guo, J.; Wu, K.; Seltmann, R.; Zhang, R.Q.; Ling, M.X.; Li, C.Y.; Zhang, L.P.; Sun, W.D. Unraveling the link between mantle upwelling and formation of Sn-bearing granitic rocks in the world-class Dachang tin district, South China. *Geol. Soc. Am. Bull.* **2022**, *134*, 1043–1064. [[CrossRef](#)]
19. Guo, J.; Zhang, G.Y.; Xiang, L.; Zhang, R.Q.; Zhang, L.P.; Sun, W.D. Combined mica and apatite chemical compositions to trace magmatic-hydrothermal evolution of fertile granites in the Dachang Sn-polymetallic district, South China. *Ore Geol. Rev.* **2022**, *151*, 105168. [[CrossRef](#)]
20. Zhang, J.; Huang, W.T.; Chen, X.L.; Wu, J.; Ren, L.; Liang, H.Y.; Chen, L. Different Geochemical Characteristics and Genetic Link between Sn-polymetallic Deposit and Skarn Zn-Cu Deposit in the Dachang Ore Field, Guangxi. *Geotecton. Metallog.* **2019**, *43*, 1186–1199. (In Chinese with English Abstract)
21. Li, M.Q. A Geochemical Study on the Fluid Inclusion of the Lamo Zn-Cu Polymetallic Deposit in Guangxi, China. *J. Guizhou Inst. Technol.* **1995**, *4*, 55–59. (In Chinese with English Abstract)
22. Fu, M.; Changkakoti, A.; Krouse, H.R.; Gray, J.; Kwak, T.A.P. An oxygen, hydrogen, sulfur, and carbon isotope study of carbonate-replacement (skarn) tin deposits of the Dachang tin field, China. *Econ. Geol.* **1991**, *86*, 1683–1703. [[CrossRef](#)]
23. Fu, M.; Kwak, T.A.P.; Mernagh, T.P. Fluid inclusion studies of zoning in the Dachang tin-polymetallic ore field. People's Republic China. *Econ. Geol.* **1993**, *88*, 283–300. [[CrossRef](#)]
24. He, L.; Liang, T.; Wang, D.H.; Zhao, Z.; Liu, B.S.; Gao, J.G.; Cen, J.B. Geochemical Characteristics of Garnet from Zinc-Copper Ore Bodies in the Changpo–Tongkeng Deposit and Its Geological Significance. *Minerals* **2023**, *13*, 937. [[CrossRef](#)]

25. Li, Y. Genesis of the Lamo Zn-Cu Deposit, Nandan, Guangxi. Master's Thesis, China University of Geosciences (Beijing), Beijing, China, 2017; pp. 1–83. (In Chinese with English Abstract)
26. Armstrong, J.T. CITZAF: A package of correction programs for the quantitative electron microbeam X-ray analysis of thick polished materials, thin Films, and particles. *Microbeam Anal.* **1995**, *4*, 177–200.
27. Fricker, M.B. Design of Ablation Cells for LA-ICP-MS. Ph.D. Thesis, ETH Zürich, Zürich, Switzerland, 2012. [[CrossRef](#)]
28. Liu, Y.S.; Hu, Z.C.; Gao, S.; Günther, D.; Xu, J.; Gao, C.G.; Chen, H.H. In situ analysis of major and trace elements of anhydrous minerals by LA-ICP-MS without applying an internal standard. *Chem. Geol.* **2008**, *257*, 34–43. [[CrossRef](#)]
29. Poldervaart, A.; Hess, H.H. Pyroxenes in the crystallization of basaltic magma. *J. Geol.* **1951**, *59*, 472–489. [[CrossRef](#)]
30. Filip, J.; Dachs, E.; Tucek, J.; Novak, M.; Bezdicka, P. Low-temperature calorimetric and magnetic data for natural end-members of the axinite group. *Am. Mineral.* **2008**, *93*, 548–557. [[CrossRef](#)]
31. Dana, E.S. *A System of Mineralogy*, 6th ed.; John Wiley & Sons Inc.: New York, NY, USA, 1924.
32. Deer, W. *Rock-Forming Minerals*; Longmans: London, UK, 1982.
33. Leake, B.E.; Woolley, A.R.; Arps, C.E.S.; Birch, W.D.; Gilbert, M.C.; Grice, J.D.; Hawthorne, F.C.; Kato, A.; Kisch, H.J.; Krivovichev, V.G.; et al. Nomenclature of amphiboles: Report of the subcommittee on amphiboles of the international mineralogical association, commission on new minerals and mineral names. *Can. Mineral.* **1997**, *35*, 219–246.
34. Armbruster, T.; Bonazzi, P.; Akasaka, M.; Bermanec, V.; Chopin, C.; Giere, S.; Heuss-Assbichler, A.; Menchetti, S.; Pan, Y. Recommended nomenclature of epidote-group minerals. *Eur. J. Mineral.* **2006**, *18*, 551–567. [[CrossRef](#)]
35. Sun, S.S.; McDonough, W.S. Chemical and Isotopic Systematics of Oceanic Basalts: Implications for Mantle Composition and Processes. In *Magmatism in the Ocean Basins*; Saunders, A.D., Norry, M.J., Eds.; Geological Society: London, UK, 1989; Volume 42, pp. 313–345.
36. Einaudi, M.T. Skarn deposits. *Econ. Geol.* **1981**, *75*, 317–391.
37. Einaudi, M.T.; Burt, D.M. Introduction; terminology, classification, and composition of skarn deposits. *Econ. Geol.* **1982**, *77*, 745–754. [[CrossRef](#)]
38. Meinert, L.D.; Hedenquist, J.W.; Satoh, H.; Matsuhisa, Y. Formation of anhydrous and hydrous skarn in Cu-Au ore deposits by magmatic fluids. *Econ. Geol.* **2003**, *98*, 147–156. [[CrossRef](#)]
39. Kwak, T.A. Hydrothermal alteration in carbonate-replacement deposits. *Geol. Assoc. Can. Short Course Notes* **1994**, *11*, 381–402.
40. Peng, H.J.; Li, H.Y.; Pei, R.F.; Zhang, C.Q.; Zhou, Y.M.; Tian, G.; Li, J.X.; Long, F. Mineralogical characteristics and metallogeny of the Hongniu-Hongshan copper deposit in Zhongdian area, Yunnan Province, China. *Acta Petrol. Sin.* **2014**, *30*, 237–256. (In Chinese with English Abstract)
41. Zhu, Q.Q.; Xie, G.Q.; Li, W.; Zhang, F.; Wang, J.; Zhang, P.; Yu, B.F. In situ analysis of garnets from the Jinshandian iron skarn deposit, Hubei Province, and its geological implications. *Geol. China* **2014**, *41*, 1944–1963. (In Chinese with English Abstract)
42. Xie, G.Q.; Mao, J.W.; Zhu, Q.Q.; Yao, L.; Li, Y.H.; Li, W.; Zhao, H.J. Geochemical constraints on Cu-Fe and Fe skarn deposits in the Edong district, Middle-Lower Yangtze River metallogenic belt, China. *Ore Geol. Rev.* **2015**, *64*, 425–444. [[CrossRef](#)]
43. Zhao, P.L.; Yuan, S.D.; Yuan, S.D. Geochemical characteristics of garnet in the Huangshaping polymetallic deposit, southern Hunan: Implications for the genesis of Cu and W-Sn mineralization. *Acta Petrol. Sin.* **2018**, *34*, 2581–2597. (In Chinese with English Abstract)
44. Ghosh, U.; Upadhyay, D. The retrograde evolution of F-rich skarns: Clues from major and trace element chemistry of garnet, scheelite, and vesuvianite from the Belka Pahar wollastonite deposit, India. *Lithos* **2022**, *422–423*, 106750. [[CrossRef](#)]
45. Zhan, Q.; Gao, X.Y.; Meng, L.; Zhao, T.P. Ore genesis and fluid evolution of the Sandaozhuang supergiant W-Mo skarn deposit, southern margin of the North China Craton: Insights from scheelite, garnet and clinopyroxene geochemistry. *Ore Geol. Rev.* **2021**, *139*, 104551. [[CrossRef](#)]
46. Massawe, R.J.; Lentz, D.R. Skarn formation and Cu-Ag mineralization in the McKenzie Gulch area, northern New Brunswick, Canada: Implication for the applications of mineral chemistry in exploration for porphyry copper and skarn deposits. *J. Geochem. Explor.* **2022**, *238*, 106965. [[CrossRef](#)]
47. Han, F.; Zhao, R.S.; Shen, J.Z. *Geology and Genesis of Dachang Tin Polymetallic Deposit*; Geological Publishing House: Beijing, China, 1997; pp. 1–213. (In Chinese with English Abstract)
48. Sanero, E.; Gottardi, G. Nomenclature and crystal chemistry of axinites. *Am. Mineral.* **1968**, *53*, 1407–1411.
49. Qian, Y.X. A study on micromorphology, chemical composition and formation condition of axinite in Gejiu. *Mineral. Petrol.* **1990**, *10*, 1–5. (In Chinese with English Abstract)
50. Hu, A.X.; Peng, J.T.; Suo, M.Y. The first discovery of axinite in the Furong tin deposit, southern Hunan: An important boron-bearing mineral and its implications for tin mineralization. *Acta Petrol. Sin.* **2023**, *39*, 1730–1742. (In Chinese with English Abstract) [[CrossRef](#)]
51. Yang, W.Q.; Zheng, X.J.; Yang, G.S.; Yan, Y.E.; Sun, B. The geological significance of vesuvianite in the Heishuigou Zn-Cu deposit in the Dachang area, Guangxi Autonomous Region, China. *Acta Mineral. Sin.* **2022**, *42*, 193–202. (In Chinese with English Abstract)
52. Chen, S.C.; Yu, J.J.; Bi, M.F.; Lehmann, B. Tin-bearing minerals at the Furong tin deposit, South China: Implications for tin mineralization. *Geochemistry* **2022**, *82*, 125856. [[CrossRef](#)]

53. Zhao, K.D.; Zhang, L.H.; Palmer, M.R.; Jiang, S.Y.; Xu, C.; Zhao, H.D.; Chen, W. Chemical and boron isotopic compositions of tourmaline at the Dachang Sn-polymetallic ore district in South China: Constraints on the origin and evolution of hydrothermal fluids. *Miner. Depos.* **2021**, *56*, 1589–1608. [[CrossRef](#)]
54. Manning, D.A.C. The effect of fluorine on liquids phase relationships in the system Qz-Ab-Or with excess water at 1kb. *Contrib. Mineral. Petrol.* **1981**, *76*, 206–215. [[CrossRef](#)]
55. Webster, J.D. Partitioning of F between H₂O and CO₂ fluids and topaz rhyolite melt: Implications for mineralizing magmatic-hydrothermal fluids in F-rich granitic systems. *Contrib. Mineral. Petrol.* **1990**, *104*, 424–438. [[CrossRef](#)]
56. Pollard, P.J.; Pichavant, M.; Charoy, B. Contrasting evolution of fluorine-and boron-rich tin systems. *Miner. Depos.* **1987**, *22*, 315–321. [[CrossRef](#)]
57. Thomas, R.; Förster, H.J.; Rickers, K.; Webster, J.D. Formation of extremely F-rich hydrous melt fractions and hydrothermal fluids during differentiation of highly evolved tin-granite magmas: A melt/fluid-inclusion study. *Contrib. Mineral. Petrol.* **2005**, *148*, 582–601. [[CrossRef](#)]
58. Hervig, R.L.; Moore, G.M.; Williams, L.B.; Peacock, S.M.; Holloway, J.R.; Roggensack, K. Isotopic and elemental partitioning of boron between hydrous fluid and silicate melt. *Am. Mineral.* **2002**, *87*, 769–774. [[CrossRef](#)]
59. Thomas, R.; Förster, H.J.; Heinrich, W. The behaviour of boron in a peraluminous granite-pegmatite system and associated hydrothermal solutions: A melt and fluid-inclusion study. *Contrib. Mineral. Petrol.* **2003**, *144*, 457–472. [[CrossRef](#)]
60. Zhao, P.L.; Chu, X.; Williams-Jones, A.E.; Mao, J.W.; Yuan, S.D. The role of phyllosilicate partial melting in segregating tungsten and tin deposits in W-Sn metallogenic provinces. *Geology* **2022**, *50*, 121–125. [[CrossRef](#)]
61. Bhalla, P.; Holtz, F.; Linnen, R.; Behrens, H. Solubility of cassiterite in evolved granitic melts: Effect of T, fO₂, and additional volatiles. *Lithos* **2005**, *80*, 387–400. [[CrossRef](#)]
62. Sui, Q.L.; Zhu, H.L.; Sun, S.J.; Chen, D.H.; Zhao, X.J.; Wang, Z.F. The geochemical behavior of tin and Late Cretaceous tin mineralization in South China. *Acta Petrol. Sin.* **2020**, *36*, 23–34. (In Chinese with English Abstract)

Disclaimer/Publisher’s Note: The statements, opinions and data contained in all publications are solely those of the individual author(s) and contributor(s) and not of MDPI and/or the editor(s). MDPI and/or the editor(s) disclaim responsibility for any injury to people or property resulting from any ideas, methods, instructions or products referred to in the content.